

Tailoring the Electrochemical Performance of rods-like Co-MOF: Fe - Derived $\text{Co}_3\text{O}_4\text{:Fe}$ Electrodes for Supercapacitor Applications



By

Maryam Shah

(Registration No: 00000365121)

**This work is submitted as MS thesis in partial fulfillment of the requirements
for the degree of**

(MS in Physics)

Supervisor By: Dr. Fahad Azad

Department of Physics

School of Natural Sciences(SNS)


National University of Sciences & Technology (NUST)


Islamabad, Pakistan


(2024)

THESIS ACCEPTANCE CERTIFICATE

Certified that final copy of MS thesis written by **Maryam Shah** (Registration No. **00000365121**), of **School of Natural Sciences** has been vetted by undersigned, found complete in all respects as per NUST statutes/regulations, is free of plagiarism, errors, and mistakes and is accepted as partial fulfillment for award of MS/M.Phil degree. It is further certified that necessary amendments as pointed out by GEC members and external examiner of the scholar have also been incorporated in the said thesis.

Signature:  _____
Name of Supervisor: Dr. Fahad Azad _____
Date: 26/09/24 _____

Signature (HoD):  _____
Date: 27-09-2024 _____

Signature (Dean/Principal):  _____
Date: 27.09.2024 _____

National University of Sciences & Technology**MS THESIS WORK**

We hereby recommend that the dissertation prepared under our supervision by: **MARYAM SHAH** Regn No. **00000365121** Titled: "**Tailoring the Electrochemical Performance of Co-MOF:Fe Derived Co₃O₄:Fe Electrode Material for Supercapacitor Application**" accepted in partial fulfillment of the requirements for the award of **MS** degree.

Examination Committee Members1. Name: DR. FAHEEM AMINSignature: 2. Name: DR. MUHAMMAD ADIL MANSOORSignature: Supervisor's Name: DR. FAHAD AZADSignature: 
Head of Department27-09-2024
Date**COUNTERSIGNED**Date: 27-09-2024
Dean/Principal

DEDICATION

To my dearest parents,

This thesis is a testament to your boundless love, sacrifices, and unwavering belief in me. From the very beginning, you nurtured my curiosity and instilled in me the values of perseverance, hard work, and resilience. Your constant encouragement and selfless support have been my guiding light through every challenge and triumph. Words cannot fully express the depth of my gratitude for all that you've done. This achievement is as much yours as it is mine, for it was your faith in my dreams that gave me the strength to pursue them.

With all my heart, I dedicate this work to you, for without you, none of this would have been possible

ACKNOWLEDGMENT

I express my profound thanks and heartfelt gratitude to Almighty ALLAH, the Creator of the Universe, and the most deserving of all praises, the Merciful, who blessed me with determination, potential, and aptitude to complete this research. I offer my humblest and sincere thanks to the Holy Prophet Muhammad (Sallallah-o-Alaih-e-Waalyh-e Wasallum), who is the source of knowledge and guidance for the entire world forever and urged his followers to seek knowledge from cradle to grave.

I wish to express heartfelt thanks to Dr. Fahad Azad my MS supervisor, for his enthusiastic support, academic guidance, invigorating encouragement, and fruitful discussions, and for providing me with all the required laboratory resources, that facilitated the efficient completion of my MS research and thesis. Furthermore, I feel highly privileged to take the opportunity to express my deep sense of gratitude to my supervisor for his extreme humbleness, reassurance, and way of counseling from time to time. I am deeply grateful for your guidance, patience, and insightful feedback throughout this research. Your mentorship has been invaluable, and your belief in my potential has motivated me to push the boundaries of my abilities. Your mentoring and instruction have improved me in every walk of life. The time I have spent with you during this research will help and guide me when I have my research group. It has been an honor to have such a cool supervisor for the rest of my life.

I'm also very thankful to my GEC members Dr. Fahim Amin and Dr. Muhammad Adil Mansoor for their useful suggestions and guidance.

I would like to express my sincere gratitude to the school administration for their generous support and provision of resources during our research. I am especially thankful to Prof. Rashid Farooq principal of SNS, and Head of the Department of Physics, Prof. Syed Rizwan Hussain for their support and for being readily available whenever needed.

TABLE OF CONTENTS

LIST OF SYMBOLS AND ABBRIVATION.	v
ABSTRACT.....	vi
CHAPTER 1: INTRODUCTION.....	1
1.1 IN OVERVIEW OF THE ENERGY STORAGE DEVICES AND MATERIALS.....	1
1.2 FUNDAMENTALS OF ENERGY STORAGE: AN OVERVIEW OF CAPACITOR.....	4
1.2.1CAPACITORS.....	4
1.2.2SUPERCAPACITOR.....	5
1.2.3TYPES OF SUPERCAPACITORS.....	6
1.2.4ELECTRIC DOUBLE-LAYERED CAPACITORS.....	6
1.2.5PSEUDOCAPACITORS	7
1.2.6HYBRID SUPERCAPACITORS.....	8
1.2ELECTROCHEMICAL CHARACTERIZATION METHODS FOR HYBRID SUPERCAPACITOR	9
1.2.1CYCLIC VOLTAMMETRY.....	10
1.2.2GALVANOSTATIC CHARGE AND DISCHARGE.....	11
1.2.3DETERMINATION OF ENERGY AND POWER CAPABILITY.....	12
1.2.4ELECTROCHEMICAL IMPEDANCE SPECTROSCOPY.....	13
CHAPTER 2: LITERATURE.....	15
2.1OVERVIEW OF METAL-ORGANIC FRAMEWORKS FOR SUPERCAPACITORS	15
CHAPTER 3: APPARATUS AND CHARACTERIZATION TECHNIQUES.....	24
3.1APPARATUS REQUIRED.....	24
3.1.1DIGITAL WEIGHT BALANCE	24

3.1.2HOTPLATE.....	25
3.1.3AUTOCLAVE.....	26
3.1.4ELECTRIC OVEN.....	27
3.1.5VACCUM OVEN.....	28
3.1.6CENTRIFUGE MACHINE.....	28
3.2CHARACTERIZATION TECHNIQUES.....	29
3.2.1X-RAY DIFFRACTION	30
3.2.2FOURIER TRANSFORM INFRARED SPECTROSCOPY.....	31
3.2.3RAMAN ANALYSIS.....	32
3.2.4SCANNING ELECTRON MICROSCOPY	34
3.2.5ENERGY DISPERSIVE X-RAY SPECTROSCOPY.....	35
3.3ELECTROCHEMICAL MEASUREMENTS.....	36
CHAPTER 4: MATERIALS AND METHODS.....	38
4.1MATERIALS.....	38
4.2SYNTHESIS OF Co-MOF: Fe.....	39
4.3SYNTHESIS OF Co ₃ O ₄ :Fe.....	39
4.4ELECTRODE SYNTHESIS.....	40
4.4.1MATERIALS.....	40
4.4.1PREPARATION OF NICKEL FOAM SUBSTRATE.....	40
CHAPTER 5: RESULTS AND DISCUSSION.....	41
5.1X-RAY DIFFRACTION.....	41
5.2FTIR ANALYSIS.....	42

5.3RAMAN SPECTRA.....	44
5.4VIBRATING SAMPLE MAGNOMETER.....	44
5.5SCANNING ELECTRON MICROSCOPY.....	45
5.6ENERGY DISPERSIVE X-RAY SPECTROSCOPY.....	47
5.7TRANSMISSION ELECTRON MICROSCOPY.....	49
5.8BET RESULT.....	50
5.9GALVANOSTATIC CHARGE-DISCHARGE.....	53
5.10CYCLIC VOLTAMMETRY.....	56
5.11ELECTROCHEMICAL IMPEDANCE SPECTROSCOPY.....	58
5.12HYBRID DEVICE.....	59
CONCLUSION.....	61
LIST OF PUBLICATIONS.....	62

LIST OF SYMBOLS AND ABBRIVATIONS

Supercapacitors	SCs
Specific energy density	E_d
Specific power density	P_d
Hybrid supercapacitor	HSC
Electric double layer capacitor	EDLC
Pseudocapacitor	PC
Metal-organic frameworks	MOFs
Specific capacitance	Q_s
Nickel foam	NF
Cyclic voltammetry	CV
Galvanostatic charge discharge	GCD
Electro-impedance spectroscopy	EIS
Equivalent series resistance	ESR
Charge transfer resistance	R_{ct}
Activated carbon	AC

Abstract:

With the increasing global demand for energy, there is a critical need for efficient and sustainable energy storage solutions. Supercapacitors (SCs) have emerged as promising candidates due to their high power density, long cycle life, and environmental friendliness. This study explores the development of iron-doped cobalt metal-organic frameworks (Co-MOFs: Fe) and their derived oxides supported on Ni foam as high-performance supercapacitor electrodes. The impact of conversion temperature on electrochemical properties of Co-MOFs: Fe derived Co_3O_4 : Fe was evaluated. The results disclosed that the conversion at 500 °C significantly enhances the surface area, specific capacitance, and charge transfer efficiency of the electrodes. It exhibited the highest specific capacity of 2135.08 F/g at a current density of 1 A g⁻¹, along with excellent cycling stability of 87%. Subsequently, an asymmetric supercapacitor was constructed with the MOF-derived Co_3O_4 : Fe at 500 °C as anode and activated carbon as cathode materials. The device exhibited a specific capacitance of 233.98 F/g at 1 A/g with an energy density of ~ 51.99 Wh/kg, power density of 500.14 kW/kg, and a significant capacity retention of 89 % over 10,000 cycles. These findings validate the potential of Co-MOF: Fe derived Fe-doped Co_3O_4 as potential materials for practical energy storage applications.

CHAPTER 1: INTRODUCTION

1.1 AN OVERVIEW OF THE ENERGY STORAGE DEVICE AND MATERIALS

The worldwide dependency on fossil fuels for energy generation has had an irreversible impact on the global economy and climate change [1,2]. Therefore, transitioning to renewable energy sources is essential because they are a more sustainable resource for future generations. Integrating renewable energy sources such as wind, solar, and hydro into the power grid can provide energy security and reduce reliance on foreign oil [3-5]. However, the sporadic nature of these energy sources necessitates the development of advanced energy storage systems (ESSs). Such ESSs not only ensure a reliable and consistent power supply but also enhance the efficiency of renewable energy sources and are critical in maintaining the supply and demand of energy [6-9]. Among all other energy storage devices (ESDs), batteries and supercapacitors (SCs) have garnered peculiar interest due to their expanding applications [10-12]. Batteries have gained prominence due to their high energy density (HED), which makes them a viable ESD for numerous applications ranging from portable electronic gadgets to electric vehicles [13]. In contrast, SCs have unrivaled high-power density (HPD) and swift charge and discharge characteristics [14]. Thus, they are a crucial component in electric buses, trains, and many other high-power applications. SCs can also serve as a reliable energy storage source for solar panels and wind turbines, where short-term energy storage is required [15]. Nevertheless, batteries and SCs cannot be considered sufficient and perfectly efficient to meet modern energy demands, as each has its limitations.

For instance, compared to SCs, batteries have a limited number of charge-discharge cycles and a comparatively low power density, which makes them unsuitable for applications requiring quick bursts of high-power output. Also, SCs have a relatively low energy density, implying they may not be ideal for applications requiring long-term energy storage [16]. It is of paramount importance to overcome the limitations of batteries and SCs to develop advanced ESSs capable of meeting emerging energy demands. The devices termed as “supercapatteries” or “hybrid supercapacitors” can be one promising solution to the problem [17]. A supercapattery or hybrid supercapacitor (HSC) arises from the hybridization of battery and SC. HSCs are fabricated by assembling a battery-grade

cathode and SC-grade anode into a single device. Thus, HSCs are enabled to generate high energy density (ED), high power density (PD), as well as longer life spans (Figure 1.1). Hence, keeping in view the escalating energy applications, significant efforts and investigations are needed to fabricate and optimize the supercapattery technology, that can be the potential sustainable ESD of the future.

The supremacy of a hybrid supercapacitor in various applications is largely reliant on the employed electrode materials because the selection of materials directly influences and determines the ED, PD, and life span of the HSC [18]. For efficient negative electrode/anode materials, materials with higher electrical conductivity, high surface area, chemical stability, electrolytic compatibility, and most importantly, low cost and ease of processing, are sought after. In this regard, carboniferous materials like carbon black, activated carbon (AC), carbon nanotubes, carbon aerogels, graphene, carbon fiber, etc. are preferred and are the subject of considerable investigation as anode materials for HSCs [19]. The positive electrode and cathode materials are of prime interest for supercapattery devices. A highly efficient cathode material must possess the same qualities as anode materials, as well as a higher energy density and a potential voltage window compatible with the negative electrode. Typically, battery-grade materials possess these characteristics, and materials such as oxides of metals, phosphates, phosphides, and sulfides have been favored as positive electrode materials for HSCs over time [20–22]. Although these materials are still an active area of study, as they tend to retain charges by ion intercalation and adsorption, which gives them a higher ED, decent specific capacity, and stability, but their low electrical conductivity and slow ion kinetics largely impede their integration into ESDs and more specifically in HSCs. Hence, efforts are currently being made to optimize these battery-grade materials. However, a transition toward the search and development of novel materials beyond those previously explored for supercapacitors may showcase unique characteristics and capabilities that can lead to potential device functionalities and architectures and outcast the limitations of existing materials.

MOFs are a prospective realm of energy storage materials [23]. MOFs consist of organic ligands with linked clusters or metal ions, resulting in a porous structure with a substantial surface area [24]. Although the first MOF was reported by Omar Yaghi and co-workers at the University of Michigan in the United States in the early 1990s [25], it has only been in recent years that MOFs

have received widespread attention and in-depth analysis for energy storage applications. For ESDs, MOFs offer a high surface area, which means that a large quantity of active material is confined in a small volume, which greatly benefits the energy storage capacity, as well as the highly porous network of the MOF's structure, which accommodates large quantities of electrolytic ions, also enhances the ESDs' capacity [26]. Moreover, MOFs offer structural tunability via altering the metal ions and organic ligands utilized during synthesis, enabling their widespread applications such as separation, gas storage, and catalysis. Since its inception, numerous 2D/3D metal-organic frameworks, MOF composites, and MOF-derived materials have been developed, bringing with them unique properties and characteristics that make them well-suited for ESSs and other applications.

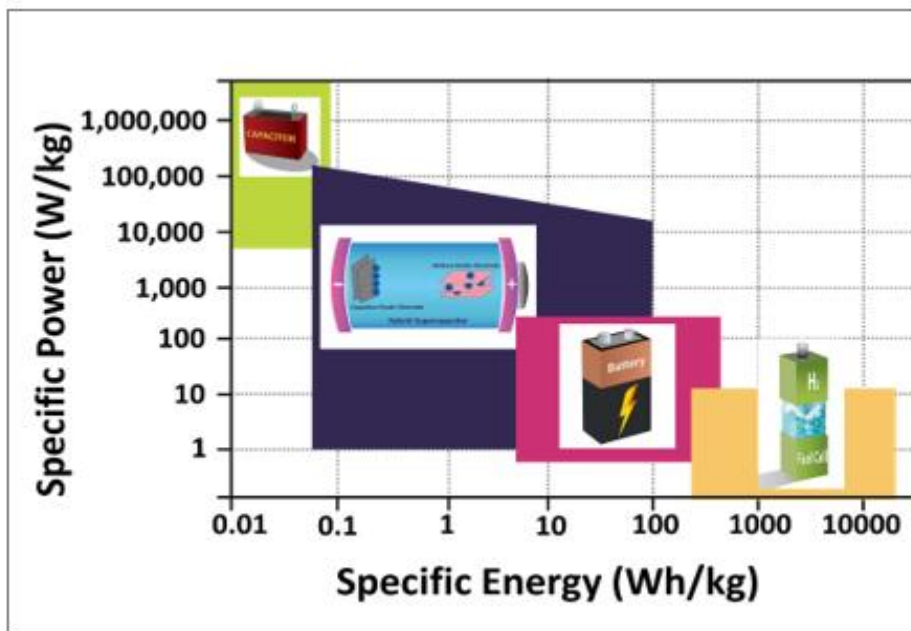


Figure 1.1. Ragone plot comparing the energy storage performance of various energy storage devices.[26]

1.2 FUNDAMENTALS OF ENERGY STORAGE: AN OVERVIEW OF CAPACITORS

1.2.1 CAPACITORS

Currently, the electronic and technological world is overflowed with capacitors of several kinds (Figure 1.2), which can be distinguished either by the type of incorporated dielectric or the charge storage phenomenon at their electrodes [27]. Much of the current energy research revolves around the advancements in capacitor technology that are capable of meeting the needs of modern energy applications by delivering enhanced stability and more specific power [28]. A conventional capacitor can only store charges in the millifarad and microfarad range, and the energy storage phenomenon is governed by the induced electric field in between the polarized dielectric medium and the electrodes [27,29]. The capacitance of conventional capacitors can be represented by the ratio of stored charge on each electrode and the applied potential to the electrode (Equation 1) [30].

$$C = \frac{Q}{V} \dots \dots \dots (1)$$

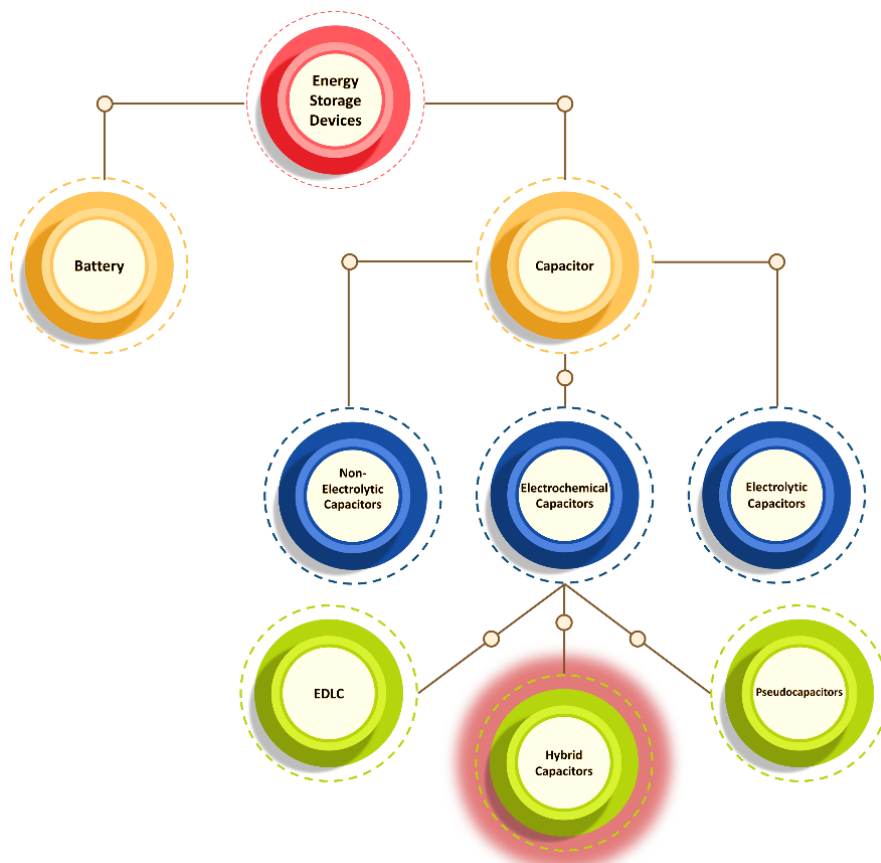


Figure 1.2. Scheme representing different types of energy storage devices.[30]

1.2.2 SUPERCAPACITORS

In essence, given the high expectations in terms of fast charging, stability, specific power, and energy of modern electric-powered devices, supercapacitor technology is like a shining star, marking its prominence in diverse domains where high as well as stable energy and power outputs are required [31]. One of the prominent features of SCs, alongside their decent energy storage and rapid power release capability, is their cyclic stability, which could be over half a million charge-discharge cycles, as SCs operation involves storage mechanisms that lack reversible redox reactions [32,33]. SCs bridge the void between the power of typical conventional capacitors and the energy of batteries by integrating electrode materials into their system that stores charges via different processes. Based on the dominant process of charge storage, SCs can be divided into three basic types: (i) electric double-layer capacitors, (ii) pseudocapacitors, and (iii) hybrid supercapacitors [34]. For convenience, these classifications of SCs are further described as follows:

1.2.3 TYPES OF SUPERCAPACITORS

Supercapacitors are categorized as EDLCs, PCs, and hybrid SCs based on their charge-storing mechanism [35-37]. The EDLCs store charges electrostatically through the double-layer electrodes [35], PCs can store charge faradaic ally via the redox reaction method at the surface of electrodes [36] while hybrid SCs store the charges both faradaically and non-faradaically [37].

1.2.4 ELECTRIC DOUBLE-LAYERED CAPACITORS (EDLCs)

EDLCs operate like conventional capacitors but for storing energy, double-layer capacitors use their interfaces (electrolyte and electrode) [38]. Moreover, these capacitors can store the charge non-faradaically and do not involve any kind of redox reaction. Therefore, no charge-shifting mechanism occurs between the electrode and electrolyte [39]. By applying the potential, charges start accumulating at the electrode surface. Through ion diffusion, the charges get stored in the pores of the electrode across the separator [40]. Normally the EDLCs store the charges electrostatically making the capacitor highly reversible as well as extremely stable without experiencing any volumetric change [41, 42].

The formation of EDLCs allows the excess or deficit of charge to be stored on the electrode interface. The oppositely charged ions start moving from the electrolyte to balance its neutrality as displayed in Figure 1.3(a) [43, 44]. By applying external potential, the electrons start moving from the negative to the positive electrode in which the cations move towards the negative electrode while anions towards the positive electrode material [39, 45]. In this process, the charge transfer did not occur between the electrodes and the electrolyte, but the electrolyte concentration always remained constant. Thus, the energy has been accumulated at the interface of the double layer [46]. To calculate the capacitance, EDLCs use Equation (2) [47]:

$$C = \frac{\epsilon_r \epsilon_0 A}{d} \dots \dots \dots (2)$$

In Equation (2), the parameter ϵ_r indicates the relative permittivity, ϵ_0 is the free space (vacuum) permittivity, A is the area between the electrodes, and d represents the thickness parameter of the double-layer capacitor. EDLCs have small double-layer thicknesses because of their inverse proportionality with the capacitance and energy of the capacitor. Due to low charge transfer resistance, the EDLCs have long cyclic life [48, 49]. Furthermore, the EDLCs mostly utilize carbonaceous materials like AC, graphene, CNTs, carbon-aerogel (CA), carbide-derived carbon (CDC), carbon fibers, and many more [41]. These materials contain a large surface area, great electrical conductivity with admirable mechanical and chemical stability. It would be worthwhile to utilize these carbon-based materials for the enhancement of the specific capacitance or to develop cheap and novel carbon materials with high capacity [50, 51].

1.2.5 PSEUDOCAPACITORS (PCs)

PCs are considered to be quite different from EDLCs as they have the capability of storing the charge faradaically and involve fast redox reaction between the electrodes and electrolyte [52]. Due to Faradic nature, they have attained higher supercapacitance and energy density than double layer capacitors. Furthermore, the PCs can store the charge by adsorption, intercalation mechanism, and by redox reaction method (oxidation and reduction reactions) [53]. The redox reaction has been used to generate the transfer of charge through the double layer as illustrated in Figure 1.3 (b) [44]. In PCs, the pseudo capacitance occurs due to thermodynamic process, change in potential, and by charge acceptance. These capacitors has the same electrical response as the EDLCs i.e., it

continuously switches its state of charge by applying the potential [37]. The capacity of the electrodes depends upon the chemical affinity of the active materials to the adsorbed ions on the electrode surface along with the dimension and structure of the electrode pores to achieve the pseudo capacitance effect [41]. Generally, the theoretical values of PC capacitance can be evaluated by the following relation:

$$C = \frac{n \times F}{M \times V} \dots \dots \dots (3)$$

where n specifies the number of electrons that are transferred during the Faradic reaction, F is the Faraday's constant, M is the molar mass of materials, and V indicates the applied potential.

Furthermore, materials used in PCs and manifesting redox reactions are conducting polymers (CPs), and metal sulfides e.g., polypyrrole (PPy), polythiophene, polyaniline (PANI), polyacetylene, and polyvinyl alcohol (PVA), etc. They also comprise transition metal oxides including RuO₂, Co₃O₄, MnO₂, V₂O₅, IrO₂, and Fe₃O₄ etc. [41]. The PCs suffer multiple challenges including low power densities because the non-faradaic process is relatively faster than the Faradic process. Moreover, the PC electrodes are more prone to change the volume during charging and discharging which reduces their mechanical strength and lowers its cyclic lifespan [54].

1.2.6 HYBRID SUPERCAPACITORS

Hybrid SCs can store the charges by comparing the capacitive electrode with the pseudocapacitive electrode as illustrated in Figure 1.3 (c) [58]. The EDLCs possess high P_s along with excellent cyclic stability and exhibit low C_s. Alternatively, PCs have shown high specific capacitance but they have low power density and cyclic stability [55]. As a result, both the Faradic and non-Faradic reactions can be used together to achieve high power densities and reduce the degradation factors of electrodes [56]. This merging of both EDLCs and PCs is known as a hybrid supercapacitor [57]. In a hybrid SC, one half acts as a double-layer capacitor and the other half as a PC. In comparison with the standard capacitors, hybrid SCs have higher energy densities along with high power densities. Such enhanced properties enable SCs to more favorable compared to any other energy storage device [58]. Most commercially available hybrid supercapacitors are asymmetric, meaning they combine two electrodes of different nature, i.e., activated carbon and MnO₂ or Ni(OH)₂ [59]. For positive electrodes of HSCs apart from oxides, several different materials have been searched for

and investigated, including metal phosphides, phosphates, sulfides, polymers, MOFs, etc. Among them, MOFs are considered to be of prime interest in recent investigations of HSCs.

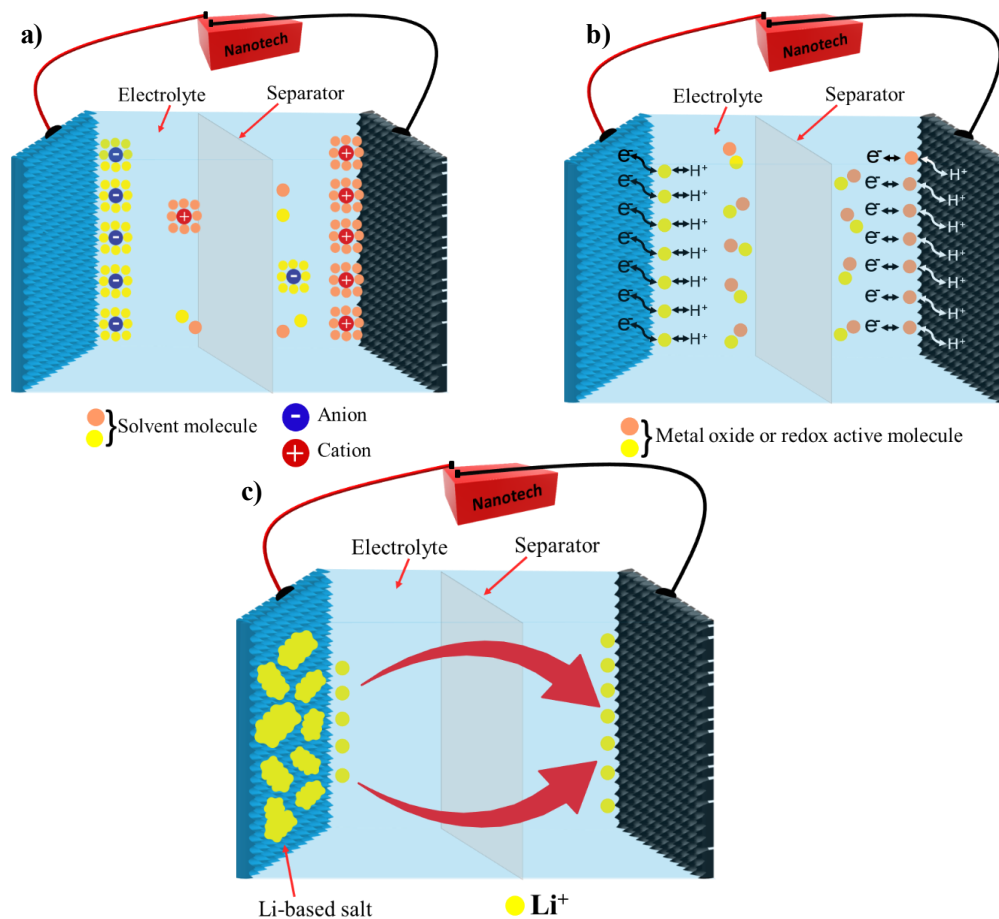


Figure 1.3. Schematic illustration of different types of supercapacitor technology, a) Electric double layer capacitor, b) Pseudocapacitor, and c) Hybrid supercapacitor.[58]

1.3 ELECTROCHEMICAL CHARACTERIZATION METHODS FOR HYBRID SUPERCAPACITORS

The electrochemical elucidation of a hybrid supercapacitor includes the evaluation of specific capacitance (C_s), specific capacity (Q_s), specific energy density (E_s), and specific power density (P_s), as well as conductivity analysis, which is also a part of electrochemical characterizations [60].

These parameters are extracted by performing experiments such as cyclic voltammetry (CV), galvanostatic charge and discharge (GCD), and electro-impedance spectroscopy analysis (EIS) [61]. These characterizations can be initialized for individual electrode materials in a three-electrode assembly comprising of a working, counter, and reference electrode, with potential being observed amongst the working electrode and reference electrode; and to investigate the hybrid supercapacitor's electrochemical characteristics, a two-electrode assembly comprising of a counter and working electrode is assembled. In such a case, voltage is taken between the positive and corresponding negative electrodes, respectively [62]. The following sections will provide intuition into the extraction of the crucial electrochemical performance parameters from CV, GCD, and EIS.

1.3.1 CYCLIC VOLTAMMETRY

Cyclic voltammetry has paramount importance in electrochemistry, as it serves as a significant tool to investigate the reaction kinetics and identify the oxidation and reduction mechanisms in a system containing molecular species. CV is also crucial to studying electrocatalysis, where reactions are driven via electron transfer [63]. Through CV analysis, the potential of the working electrode is determined versus time. Also, the current response corresponding to the dynamic potential is recorded in the form of cyclic voltammogram traces [64]. Cyclic voltammetry is usually performed in a three-electrode cell system, where the potential is taken amid the reference and working electrodes and current is measured amongst the counter and working electrode [65]. EDL, pseudocapacitive, and battery-type materials can be identified by analyzing the CV traces. The CV of typical EDLC is rectangular-shaped, while that of batteries and PCs has peaks in the CV profile attributable to the faradic redox reactions [66,67]. Figure(1.4) shows the signature CV plots of capacitive, PC, and battery-grade electrode materials. A crucial parameter in the CV experiment is the scan rate, which describes the rate at which potential is increased per second during the forward and reverse scans and is usually denoted in terms of mV s^{-1} . Furthermore, the capacitance of the electrode materials can be assessed from the cyclic voltammogram profile, which can be calculated in terms of Q_s using the equation (4):

$$Q_s = \frac{A}{mk(v_2 - v_1)} \dots \dots \dots (4)$$

Here, m , k , and v signify the active material mass, scan rate, and potential rate, respectively and A indicates the area under the voltammogram curve.

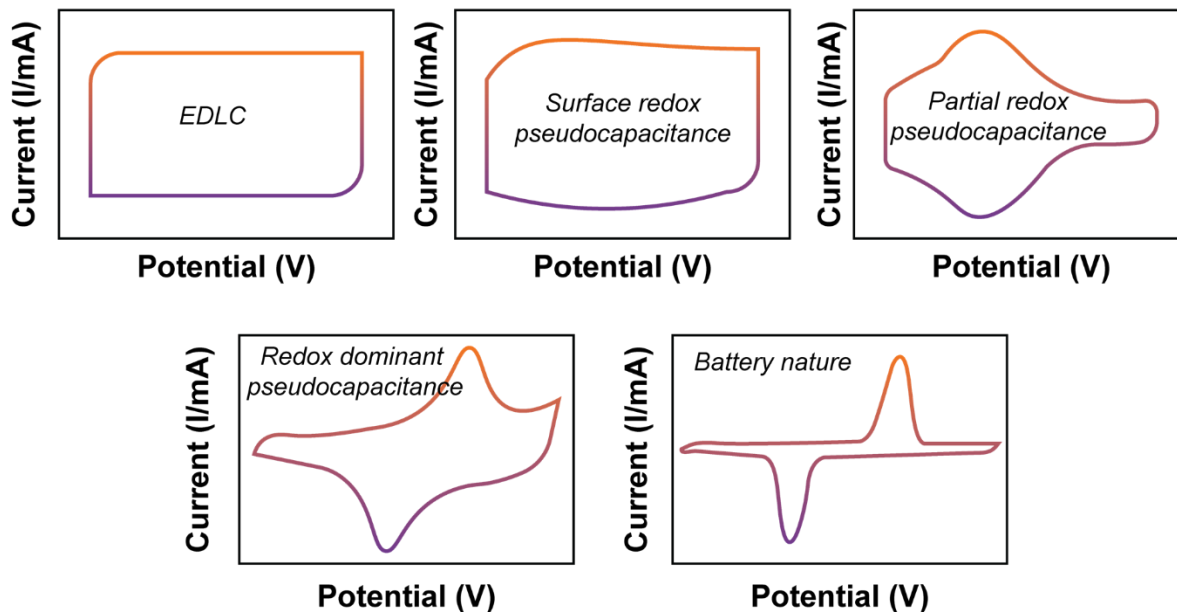


Figure 1.4. Illustrating signature CV curves of EDLC, Pseudocapacitor, and battery-natured materials.^[67]

1.3.2 GALVANOSTATIC CHARGE AND DISCHARGE

GCD analysis proves to be a fundamental electrochemical characterization that efficiently unravels several electrode characteristics such as capacitance, capacity, stability, rate capability, etc [68]. In GCD measurements, a constant CD is applied, and the response of the potential up to a specific voltage limit is monitored versus time. In PCs and HSCs, the potential window limit is always determined under the characteristics of the electrode material [69]. Figure(1.5) shows the characteristics of the GCD curves of EDLC, PC, and battery-grade materials. The specific capacitance values, denoted as Q_s , were also obtained through the GCD curves using the following equation(5): [70]

$$Q_s = \frac{I \Delta t}{m \Delta v} \dots \dots \dots (5)$$

Where I represent the current (A) Δt represents the discharging time (s), m indicates the mass loading of the prepared samples, and Δv shows the potential window for the working electrode. Capacitive-grade materials have a symmetric and linear charge/discharge curve, while pseudocapacitive and battery-grade materials show humps in the GCD profiles. However, in all cases, for optimum efficiency, the charging as well as the discharging curves should be more like a mirror image.

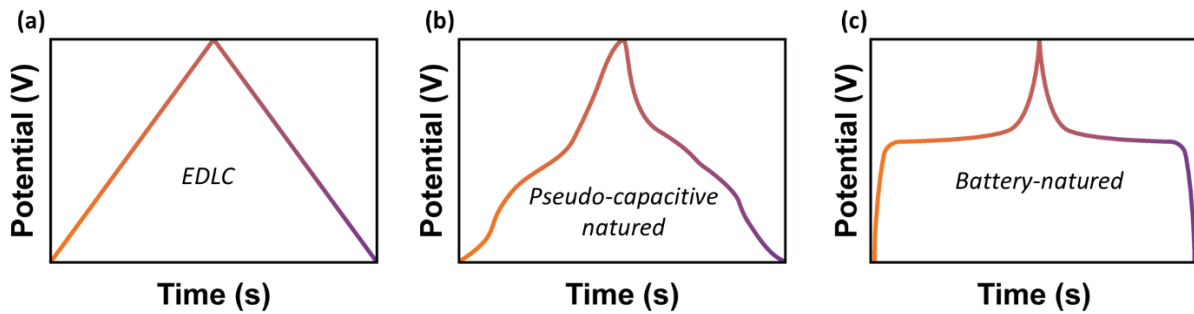


Figure 1.5. Typical GCD curves of (a) EDLC (b) pseudocapacitive material (c) battery-grade material.^[70]

1.3.3 DETERMINATION OF ENERGY AND POWER CAPABILITY

GCD analysis can efficiently aid in the calculation of energy and power density of an electrode material by employing Equation (6) and (7) [71].

$$E_d = \frac{C_s \times \Delta v}{2 \times 3.6} \dots \dots \dots (6)$$

$$P_d = \frac{E \times 3600}{\Delta t} \dots \dots \dots (7)$$

In the above equations, E_s and P_s stands for specific energy and power density, ΔV shows the potential window, C_s is the specific capacitance, and Δt is the charging/discharging time.

1.3.4 ELECTROCHEMICAL IMPEDENCE SPECTROSCOPY

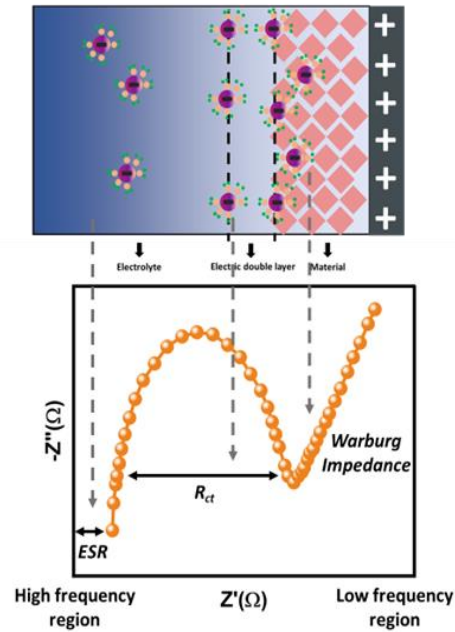
To reveal the impedance of a supercapacitor, electrochemical impedance spectroscopy (EIS) is always initialized. The voltage used for such measurements is kept within a defined range of 5–10

mV, which corresponds to frequency of 0.01 Hz–100 kHz [72]. The outcomes of EIS are attained in terms of a specific kind of plot, termed the Nyquist plot (Figure 1.6). The Nyquist plot accommodates the EIS spectra over specified frequency limits [73].

The Nyquist plot can be isolated into three regions with distinct resistance contributions [74]. The 10^4 Hz and above, higher frequency region contains a semicircle. This specific region indicates two kinds of resistances: the equivalent series resistance (ESR) and the charge transfer resistance (R_{ct} , estimated from the semicircle). The 10^5 -0.01 Hz region comprising the medium and lower frequency regions has an imaginary vertical line along the y-axis, which shows the Warburg impedance and the nature of the supercapacitor, i.e., either capacitive or Faradaic [75]. The length of the Warburg impedance determines the ion diffusion length within the electrode material. EIS measurements can also be used to estimate the capacitance as per Equation (8).

$$C = \frac{1}{2\pi f|Z|} \dots \dots \dots (8)$$

Where, f is the frequency and $|Z|$ is the impedance. Equation 8 can show the capacitance in terms of $\log |Z|$ versus $\log(f)$, which is commonly known as the Bode plot. The Bode plot depicts the relation between the frequency and capacitance to be an inverse one.



RESEARCH OBJECTIVES:

- We demonstrate a facile and cost-effective approach to design and fabricate Co-MOF:Fe derived $\text{Co}_3\text{O}_4:\text{Fe}$ at different temperatures (300 °C, 500 °C, and 800 °C) for supercapacitor applications.
- Evaluate the electrochemical performance of the derived electrodes, focusing on specific capacitance, cycling stability, and charge transfer efficiency.
- Optimize the calcination temperature to achieve the highest specific capacitance and cycling stability for enhanced supercapacitor performance.

Figure 1.6. Nyquist plot for the general understanding of EIS.^[75]

- To develop and evaluate a high-performance asymmetric device using $\text{Co}_3\text{O}_4:\text{Fe}$ as an anode and activated carbon as a cathode, with a focus on electrochemical performance, cycling stability, and energy-power density characteristics.

CHAPTER 2: LITERATURE

2.1 OVERVIEW OF METAL-ORGANIC FRAMEWORKS FOR SUPERCAPACITORS APPLICATIONS :

MOFs, a cluster of metal nodes and organic ligands, adapt unique structures in terms of large surface area, conductivity, and porosity. All of these features elevate its inclination toward energy storage devices. Apart from 2D and 3D MOFs in their pristine state, they can also induce synergistic effects by forming composites with other energy storage materials. MOFs incorporate

both organic and inorganic properties, making them a good starting point for creating a variety of metal compounds, carbon materials, and other functional materials with a significantly larger porosity. In SCs, where porous materials for the anode and cathode are still sought, MOFs could potentially prove to be an ideal candidate. To date, several pristine MOFs, their composites, and MOF-derived materials have been a center of investigation for SC applications. This section presents an inclusive examination of the recent investigations on the different classes of MOFs, which will provide a comprehensive analysis of the suitability of 2D/3D MOFs, MOF composites, and derivative materials for incorporation in SCs.

Cobalt Oxide has been discussed as a promising material and there has been quite a lot of research on it. It has been explored for its usage in energy storage devices like supercapacitors and batteries [76-78]. Cobalt oxides exist in four different forms, and among those, two of which are quite valuable for energy storage applications.

Table 2. 1 Types of cobalt oxide

Names	Formula
Cobalt (II) oxide	CoO
Cobalt (III) oxide	Co ₂ O ₃
Cobalt (IV) oxide	CoO ₂
Cobalt (II, III) oxide	Co ₃ O ₄

The most used form of Cobalt Oxide is Cobalt (II, III) oxide (CO) owing to its excellent capacitance and thermal properties [79], [80, 81]. Cobalt Oxide is also an economical material and quite abundant. It possesses a spinal-like structure which is illustrated in the figure (2.1). Co (II) ions are present. Red balls ions occupy the tetrahedral 8(a) sites, while Co (III) ions occupy the octahedral 16(d) sites.

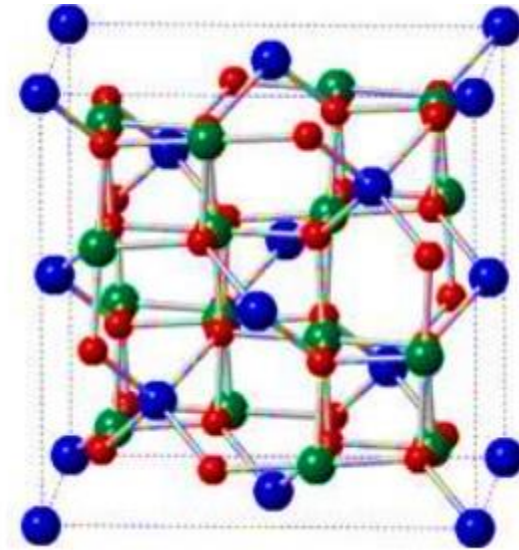


Figure 2.1.The crystal structure of Cobalt (IV) oxide [76]

Despite the advantages, there are some drawbacks associated with Cobalt Oxide, including its high resistivity, toxicity, and low charge ionic conductivity. Researchers are experimenting with numerous techniques to tackle this problem by creating a hybrid structure of Cobalt Oxide. Graphene and carbon nanotubes are the most popular nanomaterials that have been used to synthesize hybrids and they can significantly enhance the charge transport and kinetics of the material, even when used in minute amount. Poizot et al. used Cobalt Oxide as an anode for the very first time in lithium-ion batteries in 2000 [82]. Alcántara et al. then reported NiCo_2O_4 as an electrode in sodium-ion batteries in March 2002 [83]. A lot of research was conducted on the morphological properties of the supercapacitors as the capacitance value is interlinked with the morphology.

Yuan YF et al. reported the synthesis of 3D Co_3O_4 in March 2012, which consisted of a hierarchical crystal structure to be used for pseudocapacitive applications. He grew nanoflakes film of about 20nm thickness which was porous. The results showed that 443 F g^{-1} capacitance was achieved at 2 A g^{-1} [84]. Kang CW et al. in 2012 reported the synthesis of nanosheets of Co_3O_4 for supercapacitor applications, for which he employed the electrodeposition method. He used Ti as a substrate for the growth of the nanosheets. The results showed that a value of 1035 F g^{-1} was attained for the specific capacitance at 2 A g^{-1} [85]. Fin Y et al. in 2014 synthesized Co_3O_4 nanoflakes exhibiting a hierarchical crystal structure for supercapacitor applications. For its synthesis, he used the precursor precipitation technique, and the results exhibited the capacitance value of 896 F g^{-1} at 1 A g^{-1} and 79.2% capacitance retention at 40 A g^{-1} [86]. Zhang G et al. in 2013 synthesized nanowires of $\text{Co}_3\text{O}_4 @ \text{NiCo}_2\text{O}_4$ exhibiting a hierarchical structure for the supercapacitor applications. The results showed that an excellent value of aerial capacitance was achieved of about 1.97 F cm^{-2} at 4 mV s^{-1} and there was a high capacitance retention after 1500 cycles of 83.7% [87]. Hu et al. in 2014 synthesized $\text{Co}_3\text{O}_4 @ \text{MnO}_2$ having a hierarchical structure by employing hydrothermal method. The results showed that a specific capacitance of about 560 F g^{-1} was achieved at 0.3 A g^{-1} and there was an excellent capacitance retention of about 95% even after 5000 cycles. [88]. W. Fu et al. 2015 synthesized nano-flowers of ZnCo_2O_4 on Nickel foam to be used for the supercapacitor application. The capacitance of 684.9 F g^{-1} was achieved at 1 A g^{-1} and there was around 95% capacitance retention achieved after 3000 cycles [89]. Zhang et al. 2015 synthesized nano-flowers of NiCo_2O_4 on graphene foam for the application of supercapacitors, for which he utilized Chemical Vapor Deposition. The results showed that there was a specific capacitance of about 1402 F g^{-1} at 1 A g^{-1} and 77% capacitance retention was achieved at 20 A g^{-1} after 5000 cycles [90]. Huixin Chen et al. 2015 synthesized nano-sheets of $\text{ZnNiCo}_2\text{O}_4$ possessing a hierarchical structure. The results showed that a specific capacitance of 1728 F g^{-1} was attained at 1 A g^{-1} and 1512 F g^{-1} at 15 A g^{-1} , while there was a capacitance retention of 87.5% at 20 A g^{-1} [91]. Wenquin et al. in 2015 studied the properties of hierarchical core-shell nanotubes of $\text{ZnCo}_2\text{O}_4/\text{MnO}_2$. The results showed that the material gave a capacitance value of 1981 F g^{-1} at 5 A g^{-1} . Additionally, the asymmetric device was assembled, and the results were determined. The outcome revealed that the value of capacitance 158 F g^{-1} was attained at 3 mA cm^{-2} with the energy density of 41.2 Wh kg^{-1} and there was 91% capacitance retention for over 4000 cycles [92]. Zu et al. in 2014 experimented with nanowires of $\text{NiCo}_2\text{O}_4/\text{MnO}_2$. The results depicted exceptional

electrochemical properties of the material and additionally, the asymmetric device assembled showed that the capacitance of 112 F g^{-1} was achieved at 2 A g^{-1} [93]. Lau et al in 2015 synthesized hierarchical $\text{NiCo}_2\text{O}_4@ \text{NiO}$ nanowires. The results showed that the material achieved a specific capacitance of 2220 F g^{-1} and there was about 93% capacitance retention for over 3000 cycles. Additionally, an asymmetric device of $\text{NiCo}_2\text{O}_4@ \text{NiO}/\text{Activated carbon}$ was constructed, and its results depicted that an energy density of about 31.5 Wh kg^{-1} was attained and there was around 89% capacitance retention 50 A g^{-1} for over 3000 cycles [94]. Xu Y et al in 2014 synthesized porous nanowires of CoMn_2O_4 and MnCo_2O_4 . The nanowires gave exceptional results, including the capacitance value of 1980 F g^{-1} at 1 A g^{-1} and 1342 F g^{-1} at 1 A g^{-1} respectively [95]. Yan Xu in 2016 synthesized a mesoporous structure of $\text{NiCo}_2\text{O}_4@ \text{GO}$ to be used as an electrode material. The specific capacitance reached around 1211.25 F g^{-1} at 1 A g^{-1} . Moreover, an asymmetric device was constructed with RGO, which gave the values of 144.45 F g^{-1} for the capacitance at 1 A g^{-1} and 51.36 Wh kg^{-1} of energy density, meanwhile, there was the retention of capacitance was around 88% for over 2000 cycles [96]. Sahoo et al. in 2016 synthesized $\text{ZnCo}_2\text{O}_4/\text{RGO}/\text{NiO}$ nanowires. The output showed that capacitance of $1,256 \text{ F g}^{-1}$ was attained at 3 A g^{-1} and the retention of capacitance was about 80% for over 3000 cycles. [97]. Fang et al. in 2017 worked on the material CoMoO_4 which had a nanoneedle morphology. The results showed the capacitance of 1628.1 C g^{-1} at 2 mA cm^{-2} and the stability of the sample was around 90% for over 5000 cycles [98]. Hu et al. in 2017 used $\text{NiZnCo}_2\text{O}_4$ to synthesize flower-like nanowires. The output of the material exhibited a specific capacitance of around 776 F g^{-1} at 2 A g^{-1} and capacitance retention of around 91% for over 10000 cycles [99]. Wu et al in 2017 synthesized microspheres of $\text{RGO}@ \text{Mn-Ni-Co oxide}$. The results showed that the value of specific capacitance reached around 646 C g^{-1} at 1 A g^{-1} . Moreover, the constructed asymmetric device of the material with N-RGO gave an energy density of 35.6 Wh kg^{-1} and the retention of capacitance was around 77.2% for over 10000 cycles [100]. Zhao et al in 2018 synthesized $\text{FeCo}_2\text{O}_4@ \text{GF}$ having a hierarchical structure to be used as a positive electrode. The specific capacitance of 58.92 mF cm^2 was attained with $17 \mu\text{W}\cdot\text{h}\cdot\text{cm}^{-2}$ energy density. The capacitance retention reached around 87.5% for over 8000 cycles. [101]. Heet al. in 2018 synthesized hierarchical needles of $\text{FeCo}_2\text{O}_4@ \text{NiCo}$. The results showed that the material had a specific capacitance value of 2320 F g^{-1} at 1 A g^{-1} . Furthermore, its asymmetric device was assembled with activated carbon, which gave an energy density of 94.9 Wh kg^{-1} of energy density. The capacitance retention of 88.2% was achieved over 4000 cycles [102]. Fing et al. in 2019 synthesized

the nano-flakes of NiCo₂O₄/graphene hydrogel, to be used as a positive electrode. The results showed that the energy density of 71 Wh kg⁻¹ was achieved at 19.2 W kg⁻¹ power density. Additionally, the rate capability of around 92% was attained for up to 5000 cycles [103]. Subramaniam et al used a hydrothermal technique for the ternary composite of Co₃O₄ nanoparticles which was grown on MWCNTs with the addition of gold (Au) nanoparticles. These nanoparticles were then studied as electrode material for real device supercapattery applications. For real device measurements, the composite Co₃O₄-MWCNTs-Au was considered as an anode and AC as a cathode in a KOH electrolyte solution of 1 M. The Co₃O₄ and MWCNTs with mixed Au nanoparticles demonstrated outstanding capacitance retention of 91.90% for 3500 charging-discharging cycles. During supercapattery measurements, the Co₃O₄/Au@MWCNTs//AC shows 91.90% capacitance retention with coulombic efficiency of 85% after 3500 GCD cycles. The device results in high P_s and E_s of 302 W kg⁻¹ and 18.80 Wh kg⁻¹ [104]. Following a similar trend also reported cubic CuCo₂O₄ nanoparticles by using precipitating agents like NaOH and oxalic acid and used for SC applications as they express tremendous incrementation in capacitance. The oxalic acid CuCo₂O₄ has exposed the highest pseudocapacitive behavior with a C_s of 785 mAh g⁻¹ at 2 A g⁻¹ and has significant capacity with retention of 95% capacitance after 2000 charge-discharge cycles. The NaOH CuCo₂O₄ (BN) and oxalic acid CuCo₂O₄ (BO) showed significant energy and power as tabulated in Table 1. Owing to the outstanding rate capacity of the electrodes caused by shorter diffusion ions path and enhanced surface area which increases their electrochemical performance [105]. Li et al prepared the triple-shelled CuCo₂O₄ microsphere by solvothermal method followed by a calcination process. These electrode materials have shown the highest C_s of 691 F g⁻¹ at 1 A g⁻¹. Furthermore, the device had achieved high E_s and P_s as given in Table 1, and had great retention of 93% after 6000 cycles [106]. A phosphorus-based cobalt manganese oxide (P-Co₂MnO_{4-x}) was prepared by using the hydrothermal method followed by a calcination process. Adding phosphorus atoms in Co₂MnO_{4-x} improves the redox reactions and offers the electrode materials to have more electrochemical centers. The cyclic curves are similar in shape at various scan rates showing excellent rate capacity. The GCD symmetrical curves connote an ideal capacitive behavior and great reversibility of Faradic reactions. The optimized electrode material exhibits Q_s of 838 F g⁻¹ with 80.3% stability after 10,000 retentions of cycles. This device depicts maximum energy and power as mentioned in Table 1 [107]. A non-calcined method was used to fabricate Co-BTC nanowire microspheres (CBNWM) by using a step

solvothermal technique which exposed an enhanced capacity. The CBNWM showed high C_s of 657 F g^{-1} at 0.5 A g^{-1} which attributes to the fact that the MOF provided more sites for ion migration. The fabricated electrode material (CBNWM) was then studied in a two-electrode assembly with AC for asymmetric SC applications. The CV and galvanic curves at potential range from 1 to 1.5 V of the device. With the increasing scan rate, the CV curves have shown no obvious deformation while the GCD curves express highly symmetric behavior at different current densities. These results indicate the high-rate capacity of the device. Furthermore, the device has shown a long cyclic life with great stability after 5000 cycles and retained a superior capacity of 120.5%. The CBNWM//AC device achieved high E_s of 34.4 Wh kg^{-1} with lower P_s of 375.3 Wh kg^{-1} [108]. The CNTs-based materials have revealed flexible and highly conductive behavior. Ma et al reported MOFs-derived CoNiS composite. Due to the 3D structure of the composite, it leads to a rapid charge transfer capacity, exceptional electronic structure, and extra pseudocapacitive behavior. The hybrid composite has exposed high C_s of 540.6 C g^{-1} at 1 A g^{-1} with a retention of 69.9% capacity. For the hybrid SCs study, the fabricated electrode was studied with AC in two electrode cells. The cyclic curves maintained their shape with increasing scan rate, annotating the best charge-discharge performance. The GCD curves demonstrated great symmetry that indicates the superior electrochemical performance of the device with a coulombic efficiency of 86.6% at 1 A g^{-1} . The device has achieved tremendous E_s of 63.5 Wh kg^{-1} with decent P_s of 800 W kg^{-1} and maintained 83% capacitance after 10,000 GCD cycles. The inspiring performances validate the best contribution of the composite for future storage devices [109]. Bi et al. used nanosheets of thin Ni-MOFs and were implanted on a zeolite imidazolate framework (ZIF-L) for the synthesis of hierarchical $\text{Co}_3\text{O}_4@\text{Ni-MOF}$. Cobalt oxide serves as a conductive material that anchors the Ni-MOF and shortens the ion diffusion routes. Meanwhile, the Ni-MOF has provided large active sites for ions. Due to these merits, the synthesized material has shown C_s of 1980.7 F g^{-1} and Q_s 225.6 mAh g^{-1} (1 A g^{-1}). In two-electrode cells, the fabricated electrode material was studied with AC for asymmetric SC measurement. The device has revealed E_s of 37.05 Wh kg^{-1} with P_s 800 W kg^{-1} . These remarkable results show that the device can be used for high-energy storage applications [110]. Meanwhile, Nagaraju et al prepared the synthesis of hierarchical Cu (CoNi) $_2$ S $_4$ ternary composite on Ni-foam via synchronous etching and MOF precursors with multiple ion doping. The MOF-derived electrode unveiled a high capacity of 181.9 mAh g^{-1} and an areal capacity of $382.1 \mu\text{Ah cm}^{-2}$ with great stability. Due to large areal capacitance, the ternary

composite offers a large volume for storing charges and thus can be used as a high-performance energy storage device. For hybrid SC measurements, the fabricated material was studied with porous carbon as a capacitive electrode. The hybrid device attained the specific energy of 0.27 mWh cm⁻² at a power of 21.75 mW cm⁻² with cyclic stability of 95.8% retention. These results illustrate that the hybrid device can be employed for the practical applications of renewable energy [111]. Similarly, Zhang et al. fabricated a Co-BTC nanowire using a non-calcined process, and due to the nanowire symmetry, it enhanced its active sites as well as ion transfer rate. The crystal has achieved high Q_s of 657 F g⁻¹ at 5 mV s⁻¹ and retained the capacity of 81.4% over 3000 cycles. The sample was then studied with AC to make a real device for asymmetric SC applications and achieved maximum E_s and P_s of 34.4 Wh kg⁻¹ and 375.3 W kg⁻¹ [112].

Many researchers have studied Co-based MOFs and derived oxide composites, but there is a lack of study on MOF-derived doped nanostructures. Doping is an effective strategy to tune the electrical properties of materials, offering advantages over composites by ensuring uniform distribution of elements, minimizing phase separation, and modifying band structure. Furthermore, this approach also opens new avenues for research using MOF as a precursor. Therefore, it is worthwhile to investigate transition metal-based MOF-derived doped oxides for high-performance supercapacitors with long-time cycling stability. In this study, we demonstrate a facile and cost-effective approach to design and fabricate Co-MOF: Fe derived Co₃O₄: Fe at different temperatures (300 °C, 500 °C, and 800 °C) for supercapacitor applications. Herein we investigate the effect of conversion temperature on the supercapacitor performance of pristine MOF. Co-MOF: Fe derived Co₃O₄: Fe at 500 °C, demonstrated outstanding supercapacitor performance, achieving a specific capacitance of 2135.08 F g⁻¹, with high cycling stability of ~ 87%, Coulombic efficiency of around 99%, and low charge transfer resistance. This exceptional performance is attributed to the larger specific surface area of MOF and the high redox activity of the metal oxides.

Table 2.2 - Reported parameters of MOFs and derived Oxides based electrode materials.

Sr. No	Electrode material	Synthesis method	Energy density (Wh/kg)	Power density (W/kg)	Stability performance/ GCD cycles	Ref.
--------	--------------------	------------------	------------------------	----------------------	-----------------------------------	------

1.	Hierarchical Co ₃ O ₄ @Ni- MOF	-	37.05	800	75% / 10,000	[110]
2.	Co-BTC nanowire microspheres	One step solvothermal	34.4	375.3	120.5% / 5000	[108]
3.	MOFs-derived CoNiS composite	-	63.5	800	83% / 10,000	[109]
4.	Cu (CoNi) ₂ S ₄ & MOF	Synchronous etching	0.27 mWhcm ⁻²	21.75 mWcm ⁻²	95.8%	[111]
5.	Co-BTC	Non-calcined process	34.4	375.3	81.4% / 3000	[112]
6.	Co ₃ O ₄	Wet chemical	63	16200	82% / 6000	[114]
7.	Co ₃ O ₄ - MWCNTs-Au	Hydrothermal	18.80	302	91.90% / 3500	[104]
8.	CuCo ₂ O ₄ microsphere	Solvothermal	25.2	1050	93% / 6000	[106]
9.	oxalic acid CuCo ₂ O ₄	Precipitating agent	14	1985	95% / 2000	[105]
10.	P-Co ₂ MnO _{4-x}	Hydrothermal	25.18	800.07	80.3% / 10,000	[107]
11.	Zn-Co- O//NCP@CC	Hydrothermal	117.92	1490.4	94% / 5000	[113]
12.	Ni/Co-MOF	-	758	1	75/5000	[115]
13.	Co-MOF/NF	-	2 mA/cm ²	13.6 F/cm ²	80/1000	[116]
14.	CC/CoNi- MOF	-	1.01 Ccm ⁻²	2 mAcm ⁻²	78/10,000	[117]

CHAPTER 3: APPARATUS AND CHARACTERIZATION TECHNIQUES

In this section, a brief discussion is provided about the equipment used throughout the experimental synthesis procedure of both MOFs and their derived oxides. Afterward, all the necessary characterization techniques, including XRD, SEM, EDX, BET, FTIR, and CV, GCD, EIS will be discussed. These techniques are used to analyze the structural, elemental, and electrochemical properties of the material.

3.1 APPARATUS REQUIRED

The apparatus used during the experimental synthesis of MOFs and their oxides are as follows:

3.1.1 DIGITAL WEIGHT BALANCE

Digital balances are tools for accurately measuring an object's mass. Weight balances are fundamental tools in laboratories and industries, serving multiple vital purposes. One primary function is to provide precise and accurate measurements of the mass of various substances.



Figure 3.1.Image of digital weight balance

This accuracy is crucial in scientific research, where even slight differences in mass can significantly impact the outcomes of experiments and analyses.

3.1.2 HOTPLATE

Laboratory hot plates serve as a heating source to uniformly heat solutions and materials. contains a magnetic stirring system. It has a magnet inside of it, for mixing solution Paired with a magnetic stir bar.



Figure 3.2.Hot plate with a beaker containing blue solution.

3.1.3 AUTOCLAVE

For crystal growth under hydrothermal (aqueous) conditions, a specialized reaction vessel known as an autoclave is essential. In the hydrothermal method to synthesize inorganic materials for extended intervals (longer reaction time) highly corrosive salts are used. The autoclave, therefore, must be designed such that it sustains highly corrosive solvents for a very long time at high pressure and temperature. By selecting an appropriate autoclave, the primary and most vital parameter is the test pressure and temperature conditions and the resistance to corrosion at that temperature-pressure range in the given hydrothermal fluid (aqueous liquid). To prevent the decay of autoclave materials, it should be covered with nonreactive or inert materials (i.e., Teflon) from inside. Teflon has a large thermal expansion coefficient. It therefore expands and contracts more upon the heating and cooling cycle than its enclosed components. Figure 3.3. Hot plate with a beaker containing blue solution.

Characteristics of an ideal hydrothermal autoclave

- a. A perfect autoclave must be inert to acid, base, and oxidizing agents.
- b. It should be capable of tolerating high pressure and temperature for a protracted time.
- c. It should be easily assembled and disassembled.
- d. And it should be long enough to induce the specified temperature gradient, etc.



Figure 3.3.Stainless steel autoclave with Teflon bottle [118]

3.1.4 ELECTRIC OVEN

Electric ovens are used for hydrothermal synthesis and drying of materials, it provides controlled and consistent heat for various experimental and sample preparation processes



Figure 3.4.Image of an electric oven [119]

3.1.5 VACCUM OVEN

For the drying of prepared samples under a low-oxygen environment, a vacuum oven is used. In this system, material is less likely to oxidize as wet or humid material is more prone to environmental oxygen molecules. Especially when a material is heated in an open-air oxidative layer or the surface of the material gets oxidized. This apparatus is used to avoid this from happening. Figure... has the image of a vacuum oven used in our lab with a



temperature limit of up to 400 °C which can be adjusted with the help of a temperature controller, with pressure that can be adjusted up to 10⁻³ torr.

Figure 3.5.Image of Heating Vacuum Oven

3.1.6 CENTRIFUGE MACHINE

A centrifuge machine is used to separate components of a liquid mixture based on their density and sedimentation properties. The HERMLE 50 ml centrifuge machine operates on the principle of sedimentation. When subjected to centrifugal force, particles with higher density are forced to the bottom of the tube, leaving behind the supernatant, which is mostly the solvent of the solution-based substance with lower density.



Figure 3.6.Image of centrifuge machine [120]

3.2 CHARACTERIZATION TECHNIQUES

To identify the structure, surface morphology, elemental analysis, functional group, surface area, and pore size of all the prepared samples are characterized by following characterization techniques.

- X-ray diffraction (XRD)
- Fourier Transform Infrared Spectroscopy (FT-IR)
- Raman Spectroscopy
- Vibrating sample magnetometer (VSM)
- Scanning electron microscope (SEM)
- Energy Dispersive X-ray Spectroscopy (EDS)
- Transmission electron microscope (TEM)
- BET (surface area Analyzer)

3.2.1 X-RAY DIFFRACTION (XRD)

In the field of material science, X-ray diffraction stands out as a valuable technique for assessing crystal structure, phase purity, crystallite size, and recognizing a range of known and unknown compounds. It's a non-destructive method for analyzing materials. X-rays with a wavelength comparable to the size of an atom are directed onto the sample being examined. The crystal structure diffracts the rays, which are then detected by a detector positioned at an angle to the plane of incidence. The typical crystalline structure comprises stacked lattices, forming repeated 'unit cells' in a three-dimensional arrangement. Consequently, simultaneous diffraction from a set of planes may stem from the first, second, and third layers. The diffracted radiation arising from the crystal structure, exhibiting both i) identical phase and ii) a wavelength variance in integral multiples of λ , has the potential for constructive overlap. However, this scenario needs to satisfy the following condition.

$$2d\sin\theta = n\lambda \text{ (referred to as Bragg's equation)}$$

The specific directions that appear as dots on the spreading pattern are referred to as reflections. XRD patterns result from electromagnetic rays hitting a widely dispersed array. Diffraction images are created using electromagnetic rays because they have a wavelength (λ) that is roughly equivalent to the distance (d) between the crystals. Diffraction occurs only when Bragg's law satisfies the criteria for producing interference of planes with distance " d ".



Figure 3.7. Image of XRD machine

3.2.2 FOURIER TRANSFORM INFRARED SPECTROSCOPY (FT-IR)

FTIR Spectroscopy explores the interaction and behavior of light or electromagnetic radiation with matter. IR spectroscopy specifically entails directing infrared photons through a sample, where the sample absorbs some infrared light and transmits the rest. The resultant spectrum reveals the molecule's absorption and transmission characteristics, creating a distinctive molecular fingerprint. Like fingerprints, each molecule configuration generates a unique infrared spectrum, enabling diverse applications for IR spectroscopy. The IR spectrum of a material is like its unique fingerprint, displaying absorption peaks that correspond to the frequency of vibrations between the bonds of the atoms in the material. Since each substance is composed of a specific set of atoms, no two compounds have the exact same IR spectrum. As a result, IR spectroscopy can be employed for the positive identification of various substances. Moreover, the intensity of the peaks in the spectrum offers insights into the quantity of material present.

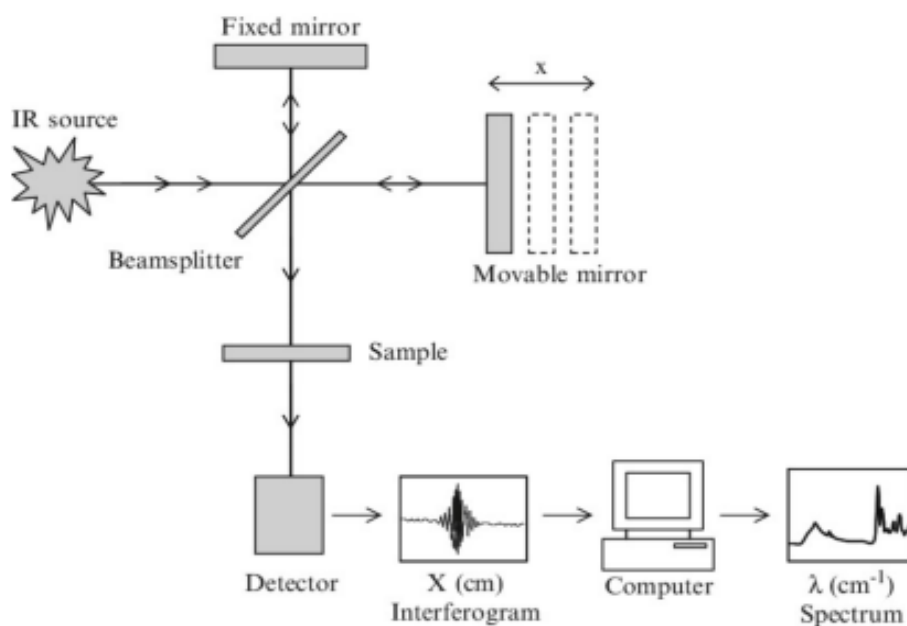


Figure 3.8. Working of FTIR spectrometer [121]

3.2.3 RAMAN ANALYSIS

Raman Spectroscopy is an optical analysis that is non-destructive to the material and gives us a lot of information about the chemical structure of material along with its phase, crystallinity,

polymorphy and molecular interactions. A monochromatic light source, usually a laser, is directed onto a sample. When photons from the light source interact with the sample, some are scattered at different wavelengths due to the molecular vibrations and rotations in the material. This scattered light, known as Raman scattering, is collected and analyzed, generating a Raman spectrum. This spectrum provides detailed information about the vibrational modes of the molecules in the sample, enabling scientists to identify and characterize different materials. The simple schematics are shown in figure. (3.9).

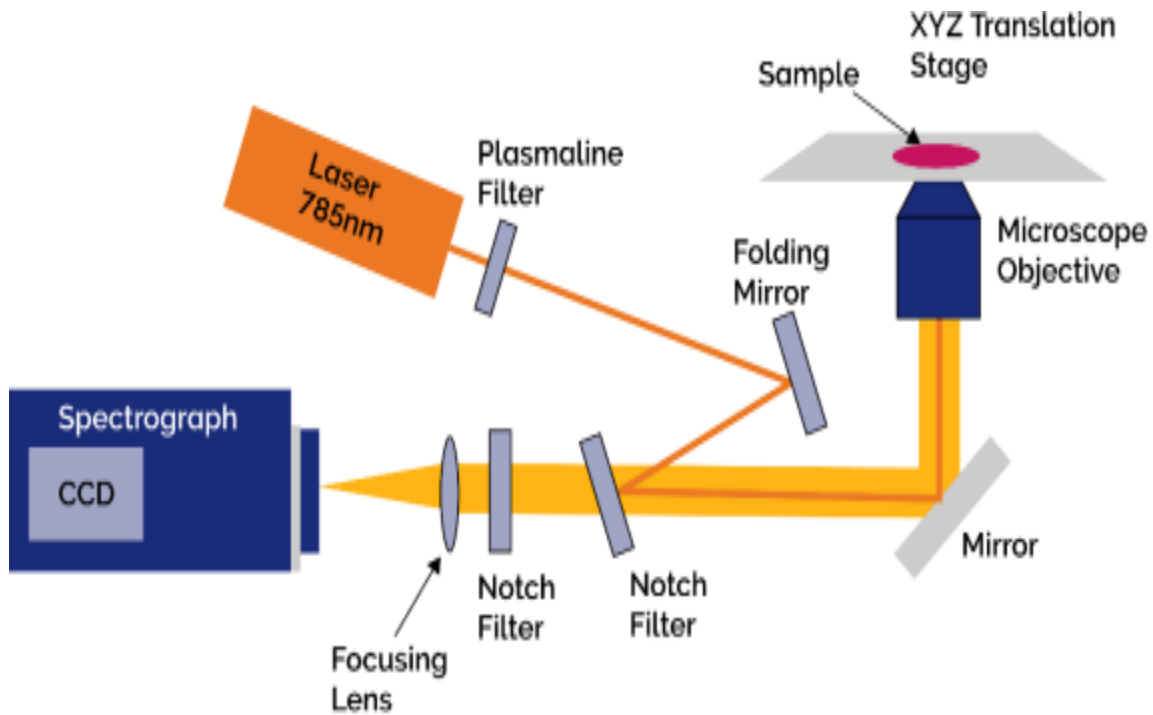


Figure 3.9. Raman spectroscopy schematic [122]

The chemical bonds present inside the material interact with the laser light and give us the required information on the screen. There are two types of laser light one is called green laser light (532 nm) and the other is called blue laser light (477 nm) which can be used for excitation. A filter then filtered the Raman Stokes from Raleigh and anti-stoke parts after deexcitation and further, the Raman shifts are recorded and then shown on the screen after decoding.

3.2.4 SCANNING ELECTRON MICROSCOPY (SEM)

SEM is a type of electron microscope that gives the image of the sample by scanning it with a high-energy beam of electrons in a raster scan pattern. SEM gives the surface morphology of the materials and generates an electron beam within a vacuum. This beam undergoes collimation through electromagnetic condenser lenses, subsequent focusing via an objective lens, and then scanning across the sample using electromagnetic deflection coils. The primary imaging technique involves capturing secondary electrons (SE) released by the material. These electrons are revealed by a luminescent material that emits light flashes when hit by electrons. These flashes are then detected and amplified by a photomultiplier tube. By correlating the sample's scan position to the resultant signal, an image is generated, closely resembling what would be observed through an optical microscope. The resulting shadowing and illumination exhibit a natural-looking surface topology. In a Scanning Electron Microscope, the electron gun serves as the source for the probing electron beams.

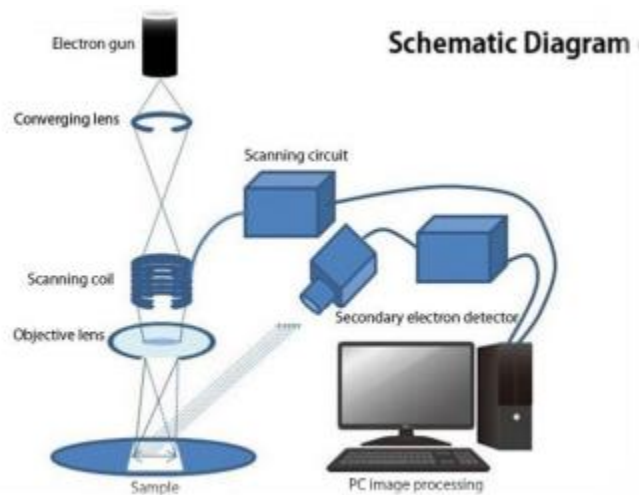


Figure 3.10.Schematic diagram of SEM [124]

Electrons are emitted from the cathode, accelerated through an electric field, and focused to form the primary image of the source. The apparent source's shape and size, beam acceleration, and current play pivotal roles in determining the SEM's performance and resolution. Typically, SEM offers magnification ranging from 20x to 30,000x with a special resolution of 50-100nm, enabling scanning of areas varying from one centimeter to five micrometers. [123]

3.2.5 ENERGY DISPERSIVE X-RAY SPECTROSCOPY (EDX)

EDX analysis is used to determine the elemental composition of a material. It involves equipping an SEM instrument with an additional X-ray detector to collect radiation from the sample's internal part. In EDX analysis, a substantial amount of energy is necessary to enable the penetration of the sample by the electron beam. The interaction between the electron beam and the sample leads to the ejection of electrons from the lower shell (K and L) of the atoms, resulting in the creation of vacancies. To fill these vacancies, electrons from higher orbitals transition to lower orbitals, emitting X-ray radiation in the process. Inner shell transition from each element gives rise to characteristic energy value. By comparing the energy of the obtained X-ray with the known data one can specify it to a known element. Fig. (3.11) represents the explanation of the phenomenon of EDX.

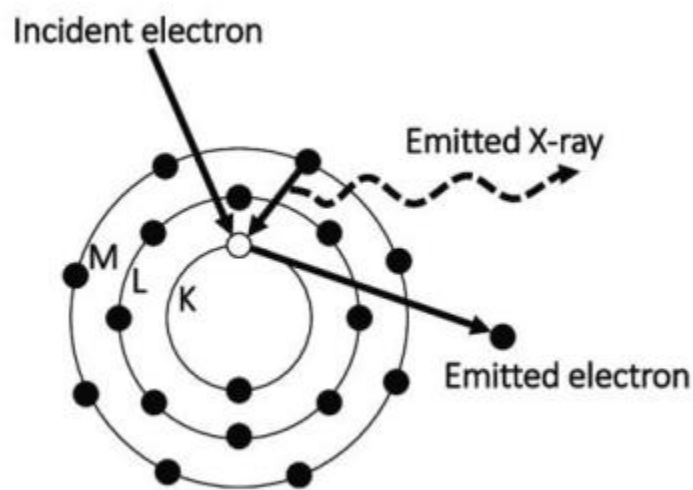


Figure 3.11.Schematic explaining EDX phenomenon [125]

3.3 ELECTROCHEMICAL MEASUREMENTS

To achieve this objective, measurements are conducted using the GAMRY 1010B Potentiostat with a three-electrode system. The potentiostat operates by applying a controlled voltage to

the working electrode, ensuring it remains at a specific potential relative to the reference electrode. This configuration enables precise measurement and analysis of the current flowing through the electrochemical cell. This process yields crucial information about redox reactions, electron transfer processes, and reaction kinetics. A working electrode, a counter electrode, and a reference electrode compose the three-electrode system. The reference electrode is essential for monitoring and correcting the voltage of the working electrode while carrying no current. At low current density, the reference electrode must maintain a constant electrochemical potential. The potential drop between the reference and working electrodes is greatly decreased due to the limited current travelling through the reference electrode. This configuration guarantees a constant reference potential and compensates for any potential dip in the solution, resulting in precise and trustworthy readings.

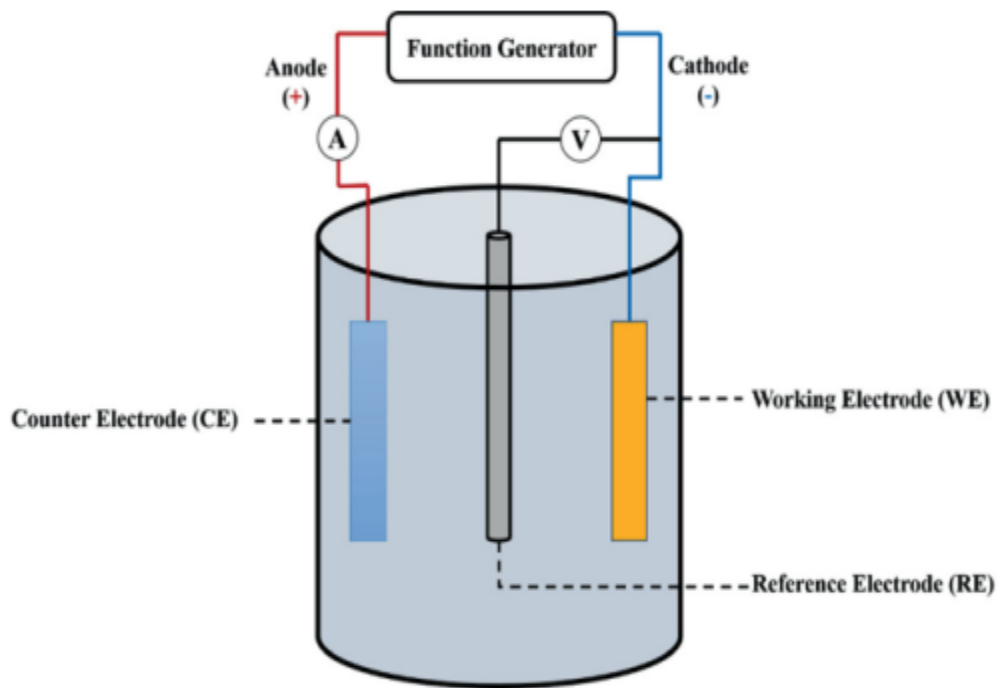


Figure 3.12. Three electrode system representation_[126]

Following is the characterization techniques were used using this Potentiostat:

- Cyclic Voltammeter (CV)

- Electrochemical impedance spectroscopy (EIS)
- Galvanostatic charge-discharge (GCD)
- GCD stability.

CHAPTER 4: MATERIALS AND METHODS

4.1 MATERIALS

All the following chemicals were used without any further purification and treatment for the synthesis of the desired sample, Cobalt nitrate hexahydrate $\text{Co}(\text{NO}_3)_2 \cdot 6\text{H}_2\text{O}$ iron nitrate nano hydrate ($\text{Fe}(\text{NO}_3)_3 \cdot 9\text{H}_2\text{O}$) 1, 4 -Benzene dicarboxylic acid /terephthalic acid (H 2BDC), N, N Dimethylformamide (DMF), sodium hydroxide (NaOH), Deionized (DI) water and ethanol were acquired from Sigma Aldrich. potassium hydroxide (KOH), hydrochloric acid (HCL), and Nafion binder were being used during the synthesis process.

The material synthesis was accomplished via an electric oven and Centrifuge was used for washing. Later, the synthesized materials were executed in a muffle furnace for annealing. The platinum wire as counter and Ag/AgCl as reference electrode have been used.

4.2 SYNTHESIS OF Co -MOF :Fe

We employed Yuen Luo and Xiaodong Yang's one-step hydrothermal technique to synthesize iron doped cobalt metal oxide (Co -MOF :Fe) with a minimal molecular weight. To prepare Solution A, 3 mmol of BD C was added to 25 mL of N, N-dimethylformamide (DMF). Similar to that, solution B was prepared by mixing 2.5 mmol of cobalt nitrate hexahydrate $\text{Co}(\text{NO}_3)_2 \cdot 6\text{H}_2\text{O}$ and 0l. 5 mmol of iron nitrate nano hydrate ($\text{Fe}(\text{NO}_3)_3 \cdot 9\text{H}_2\text{O}$) in 25 mL of ethanol solution. Separately, Sol A and Sol B were stirred for five minutes. The outcome solution was allowed to sit for 15 minutes and then stirred for 25 minutes at room temperature. After that, 2 mL of 0. 4 M NaOH that had been dissolved in ethanol was added dropwise into the solution above and stirred for an additional 5 minutes. The resulting mixture was transferred into a Teflon beaker and autoclaved for six hours at 150 °C. The resulting product was dried at 60 °C for 24 hours after being repeatedly cleaned with DM F and ethanol.

4.3 SYNTHESIS OF Co₃O₄ :Fe

For the Co₃O₄:Fe synthesis the obtained grain product was put into six alumina crucibles and calcined separately at different temperatures of 300 °C, 400 °C, 500 °C, 600 °C, 700 °C and 800 °C in a muffle furnace for three hours. The final product was allowed to cool down to ambient temperature. A black powder was obtained for the sample that was annealed at different temperatures.

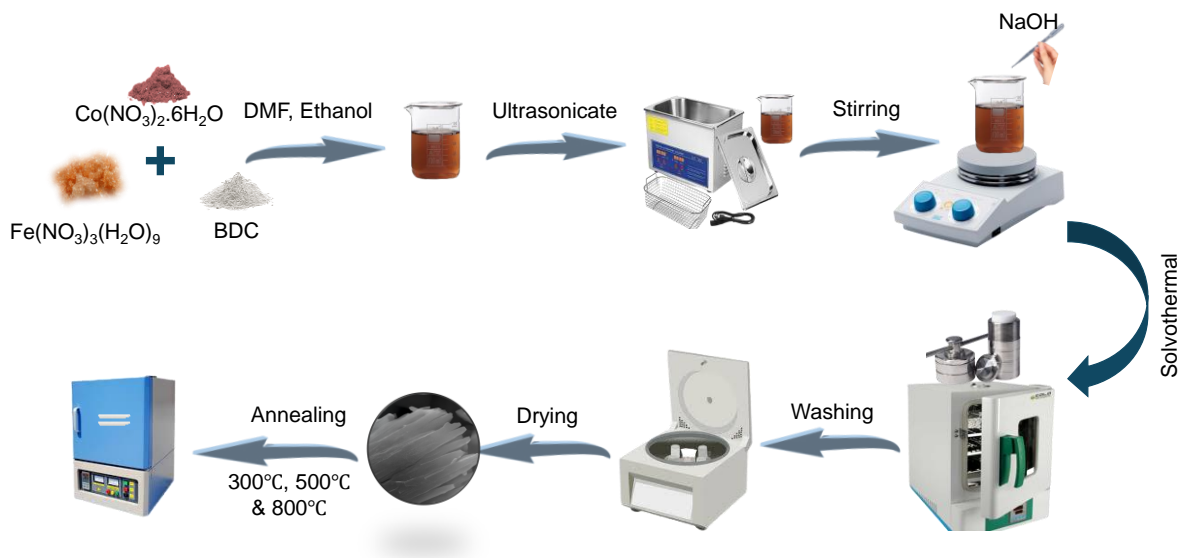


Figure 3.1. Schematic diagram of the preparation of the desired electrocatalysts

4.4 ELECTRODE SYNTHESIS

4.4.1 MATERIALS

Nickel foam (substrate), Nafion (binder), Ethanol(solvent), Deionized water (for washing), HCl (for washing).

4.4.2 PREPARATION OF NICKEL FOAM SUBSTRATE

Nickel foam was cut into 1 cm x 1.5 cm dimensions then cleaned it sonication in HCl (2-3 minutes), ethanol for 10 minutes, followed by deionized water for 10 minutes. Dry the cleaned nickel foam at 60°C in an oven or on a hot plate for 2 hours.

Slurry of Catalyst

Take 2mg of catalyst powder and add 2 drops of nafion and 3 to 4 drops of ethanol to it. Sonicate the mixture for 30-40 minutes. Take a micropipette and add slurry on the nickel foam by using a micropipette in 1 cm x 1 cm dimension. Dry the foam at 60°C in an oven for 12 hours. Cover the dried nickel foam with butter paper and aluminum foil and press it with the weight of 500 N for 5 seconds.

CHAPTER 5: RESULTS AND DISCUSSION

The structural properties of Co-MOF: Fe a bimetallic metal-organic framework along with its derivatives Co_3O_4 : Fe at 300°C, 500°C, and 800°C were evaluated using various techniques. X-ray diffraction (XRD) was used to examine the impact of annealing on crystal structures of Co-MOF: Fe. Fourier transform infrared spectroscopy (FTIR) was employed to identify the functional groups in the Co-MOF: Fe and its derivatives. Brunauer-Emmett-Teller (BET) analysis measured the surface area, pore size, and pore volume. Scanning electron microscopy (SEM) and energy dispersive X-ray spectroscopy (EDX) were utilized to observe the surface morphology and elemental analysis respectively. To further investigate the internal structural properties transmission electron microscopy (TEM) was utilized.

5.1 X-RAY DIFFRACTION (XRD)

XRD was used to analyze the structural properties of the synthesized and annealed electrocatalysts. The obtained results are shown in Fig. (5.1). The diffraction pattern of Co-Fe-MOF shows peaks at 2θ values of 8.8°, 12.4°, 15.7°, 17.5°, and 32.7° indicating its crystalline nature. These peaks showed close agreement with already reported data on Co-BDC-MOF. The absence of Fe-BDC MOF-based peaks indicates the presence of Fe in the structure of Co-MOF. The annealing was performed to decompose Co-MOF: Fe into Co_3O_4 : Fe at different temperatures. The sample annealed at 300°C showed incomplete conversion of MOF into Co_3O_4 : Fe along with a broad hump at 13.7° indicating the presence of graphitized carbon. When the annealing temperature was increased to 500°C, a relatively higher conversion of the precursor MOF to Co_3O_4 : Fe was observed. No additional peak relating to carbon in this sample indicates significant removal of BDC at this temperature. Further increasing the temperature to 800 °C resulted in the complete conversion of precursor MOF to Co_3O_4 : Fe indicated by relatively stronger diffraction peaks of cobalt oxide. The obtained diffraction peaks can be indexed as (111), (220), (311), (400), (511), and (440) (JCPDS card no. 01-078-1969) corresponding to the cubic structure Co_3O_4 . The lower intensity of diffraction peaks indicates the poor crystallinity of Co_3O_4 : Fe which might be due to the requirement of the large surface-to-volume ratio for the removal of organic linker during the transformation process.

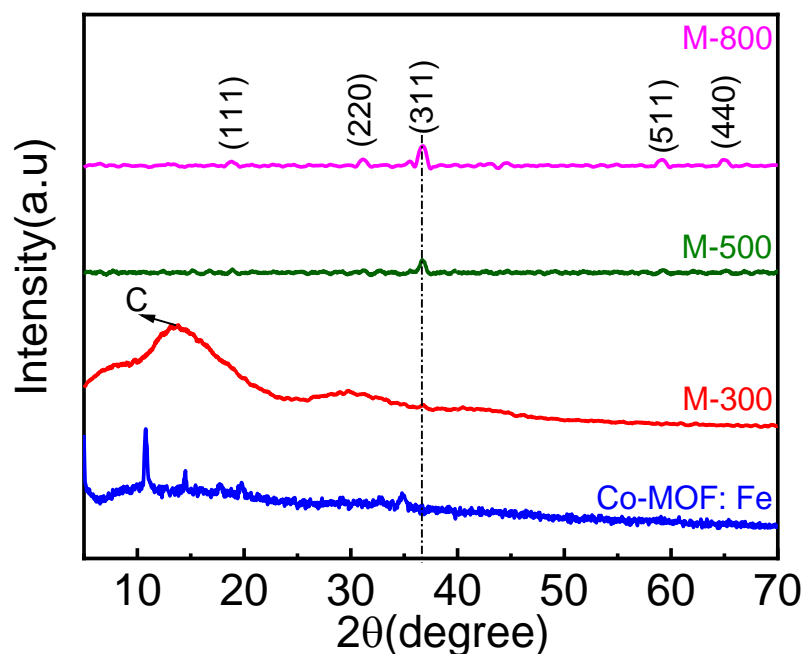


Figure 5.1. XRD pattern of all the prepared electrocatalysts.

5.2 FTIR ANALYSES

Fourier transmission infrared (FTIR) spectroscopy is used to investigate the functional group in the synthesized samples, the data as shown in Fig. (5.2). The vibrational bands at 680 cm^{-1} and 558 cm^{-1} can be attributed to the vibrations of Co(III)-O bonds and Co(II)-O stretching, respectively, in Co-MOF and derived doped oxides. Moreover, the sharp peaks around 1582 cm^{-1} and 1357 cm^{-1} in Co-MOF: Fe and the sample and the Co_3O_4 : Fe derived at $300\text{ }^\circ\text{C}$ show symmetric and asymmetric stretching vibrations of the -COOH which indicates the presence of BDC in these samples. The vibrational bands associated with -COOH were not observed in the Co_3O_4 : Fe samples derived at temperatures higher than $300\text{ }^\circ\text{C}$ showing the considerable decomposition of BDC at elevated temperatures. The band at 811 cm^{-1} was only observed in Co-MOF: Fe which can be ascribed to C-H stretching modes of the benzene ring in BDC. A broad hump around 3430 cm^{-1} was detected in all the samples indicating the hygroscopic nature of these samples. Two sharp peaks around 3624 cm^{-1} and 3588 cm^{-1} in the pristine and $300\text{ }^\circ\text{C}$ derived samples correspond to

the O–H group found in BDC, however, with the increase in the annealing temperature these bands were removed confirming the decomposition of BDC structure in this sample.

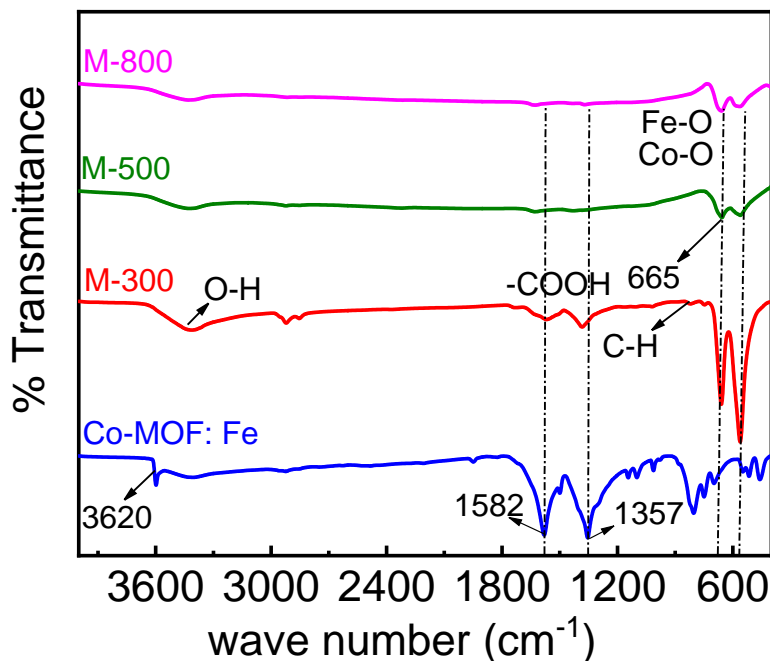


Figure 5.2. FTIR spectrum of all the prepared electrocatalysts.

5.3 RAMAN SPECTROSCOPY

Raman spectroscopy was used to determine polarizability-sensitive vibrational modes present in materials for further insights into their molecular structure and composition. The two broad bands observed at ~ 599 cm⁻¹ and ~ 1100 cm⁻¹ in the Raman spectra of all annealed samples as shown in Fig. (5.3). The band at ~ 599 cm⁻¹ is attributed to the T_{2g} mode of the Co₂O₃ structure, while the band at ~ 1100 cm⁻¹ is associated with the Co(II)-O vibration present in Co₃O₄. The presence of these modes confirms the structural presence of Co₂O₃ and CoO structures present in Co₃O₄. Additionally, the same vibrational modes in the pure Co-MOF: Fe sample suggest the presence of Co(III)-O and Co(II)-O vibrations in the Co-MOF structure, a finding that is consistent with the literature. Furthermore, there is no separate peak for Fe-MOF that further confirms the absence of Fe-MOF as a separate phase.

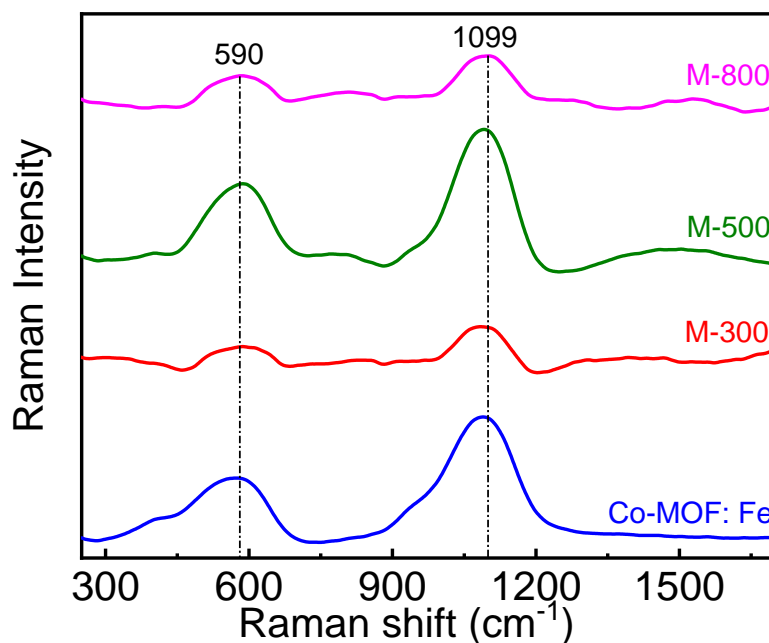


Figure 5.3. Raman spectroscopy of all the prepared electrocatalysts.

5.4 VIBRATING SAMPLE MAGNETOMETER (VSM)

VSM was utilized to analyze the magnetic properties of the synthesized samples at room temperature under an applied magnetic field of ± 20 kOe. Fig. (5.4) illustrates the hysteresis behaviors of Co-MOF: Fe, and Co-MOF: Fe-derived Co_3O_4 : Fe at different annealing temperatures. Co -MOF: Fe displays paramagnetic behavior due to the presence of BDC as an organic linker in the MOF structure. Whereas the derived Fe-doped Co-oxide at 300 °C, 500 °C, and 800 °C form a hysteresis loop with a coercivity value of 348.76 A/m, 1073.67 A/m, and 1970.04 A/m. These results indicate that derived Co_3O_4 : Fe at 300°C has a soft magnetic nature, whereas derived Co_3O_4 : Fe at 500°C and 800°C has a semi-hard magnetic nature. The soft magnetic nature of Co_3O_4 : Fe-300 °C indicates its incomplete conversion from MOF which changes to the characteristic semi-hard magnetic nature of Co_3O_4 : Fe as reported in other literature. The obtained results further confirm the synthesis of MOF-derived Fe-doped Co_3O_4 .

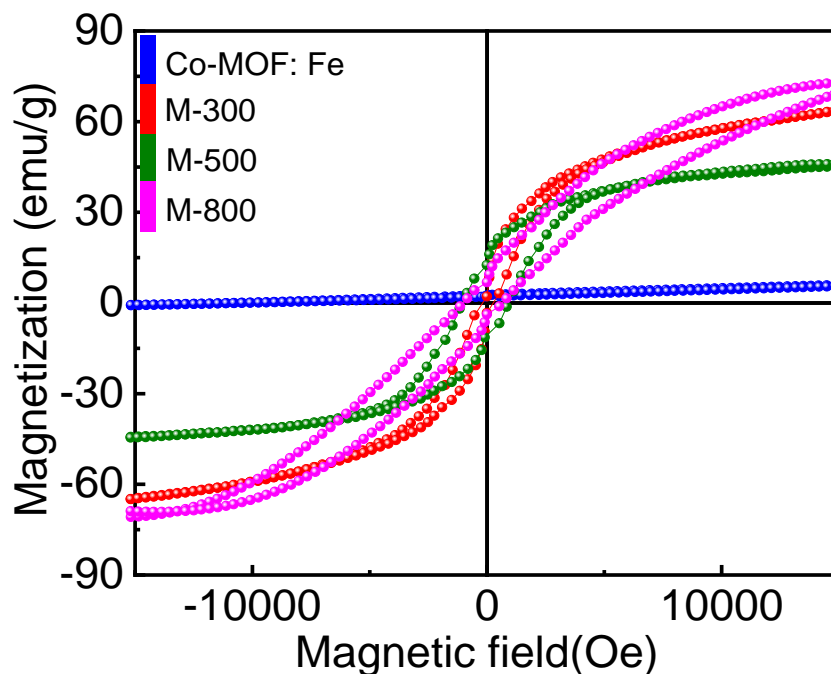


Figure 5.4. VSM graph of all the prepared electrocatalysts.

5.5 SCANNING ELECTRON MICROSCOPY (SEM)

Scanning electron microscopy (SEM) was performed to analyze the morphology of Co-MOF: Fe, and derived Co_3O_4 : Fe at 300°C, 500°C, and 800°C. The micrographs of these samples are shown in Fig. 5.5(a-d). Co-MOF: Fe exhibits rod-shaped morphology indicating the porous nature of its particles (Fig. 5.5 (a)). The SEM micrograph of Co_3O_4 : Fe-300 shows that pyrolysis at 300 °C has introduced irregularities in the rod-shaped morphology of Co-MOF: Fe. Moreover, the retained morphological characteristic of precursor MOF in this sample indicates the incomplete conversion of the MOF into derived Co_3O_4 : Fe, which is also revealed by XRD results. The SEM image of Co_3O_4 : Fe-500 shows agglomerated nanoparticles, demonstrating that the rod-shaped morphology of the Co-MOF: Fe was destroyed when the pyrolysis was carried out at 500 °C. The further increase in pyrolysis temperature leads to grain growth, forming micron-sized irregularly shaped particles of Co_3O_4 : Fe, as shown in Fig. 5.5 (c).

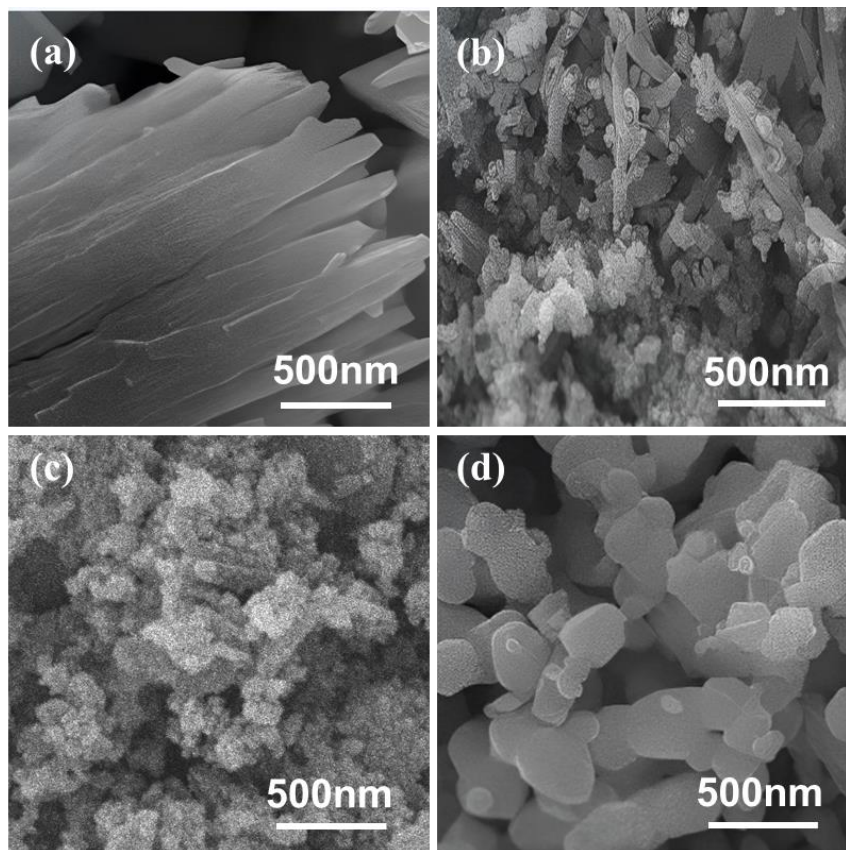


Figure 5.5.(a-d) SEM micrographs illustrating the morphological evolution of (a) Co-MOF: Fe and its derived Co_3O_4 : Fe after pyrolysis at (b) 300°C , (c) 500°C , and (d) 800°C . (a) Co-MOF: Fe exhibits a rod-shaped morphology; (b) The SEM image of Co_3O_4 : Fe-300 reveals retained rod-shaped features with introduced irregularities, suggesting incomplete conversion from the MOF precursor; (c) Co_3O_4 : Fe-500 shows agglomerated nanoparticles, indicating the destruction of the initial rod-shaped morphology.

5.6 ENERGY-DISPERSIVE X-RAY SPECTROSCOPY(EDX)

Energy-dispersive X-ray spectroscopy mapping a valuable analysis for analyzing elemental presence and distribution within a synthesized sample. EDX analysis was conducted on all samples, with results and colored elemental maps displayed in the Figure.5.6(a-d). The C, O, Co, and Fe were identified in Co-MOF:Fe, Co_3O_4 :Fe-300, Co_3O_4 :Fe-500 and Co_3O_4 :Fe-800 and their

respective weight percentages are detailed in the tables included in Figures presents the EDS results.

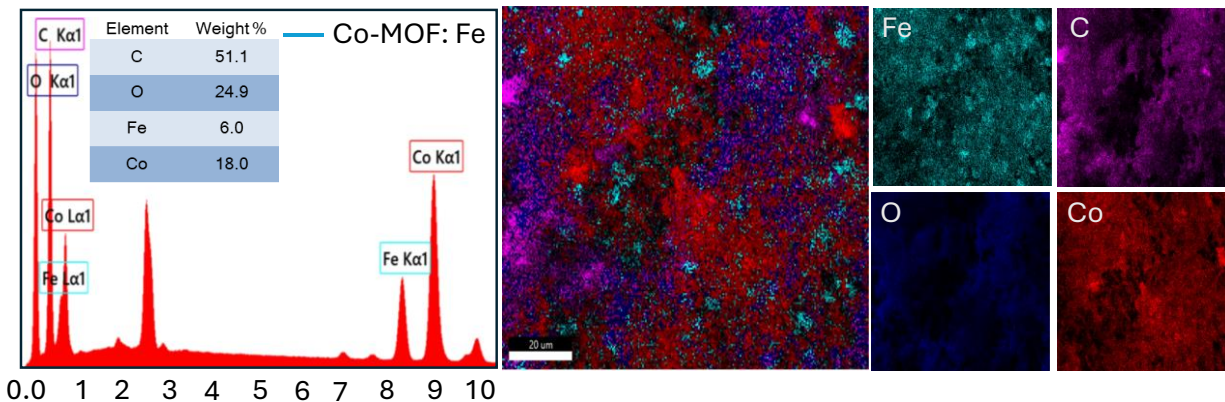


Figure 5.6.(a) EDX graphs of Co-MOF:Fe.

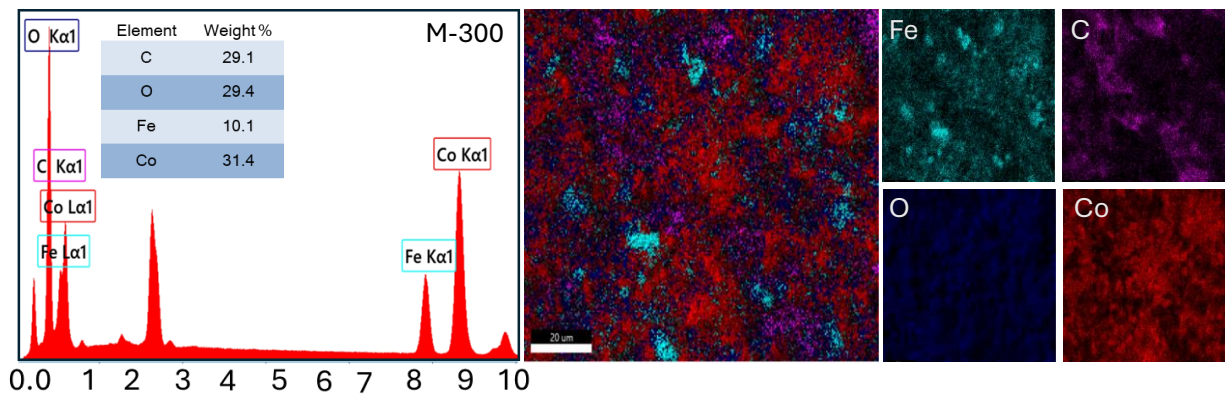


Figure 5.6.(b) EDX graphs of Co₃O₄:Fe-300.

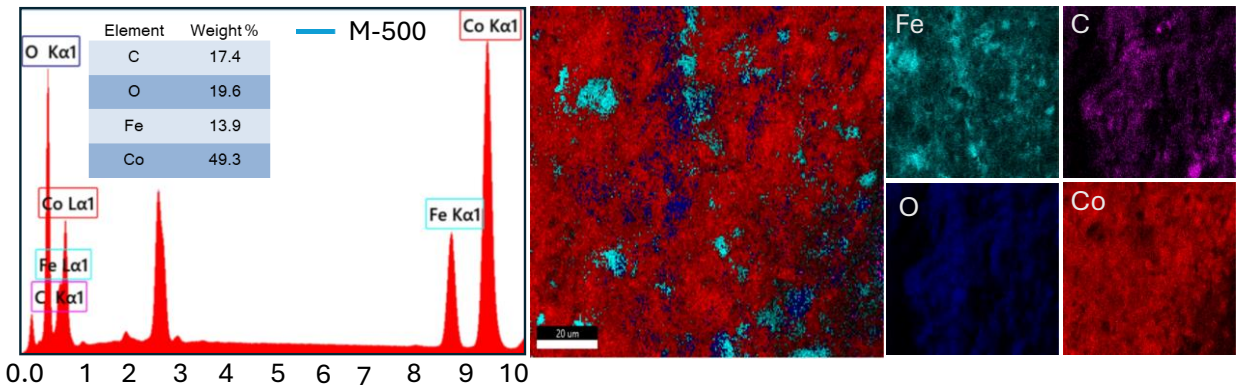


Figure 5.6.(c) EDX graphs of $\text{Co}_3\text{O}_4\text{:Fe-500}$.

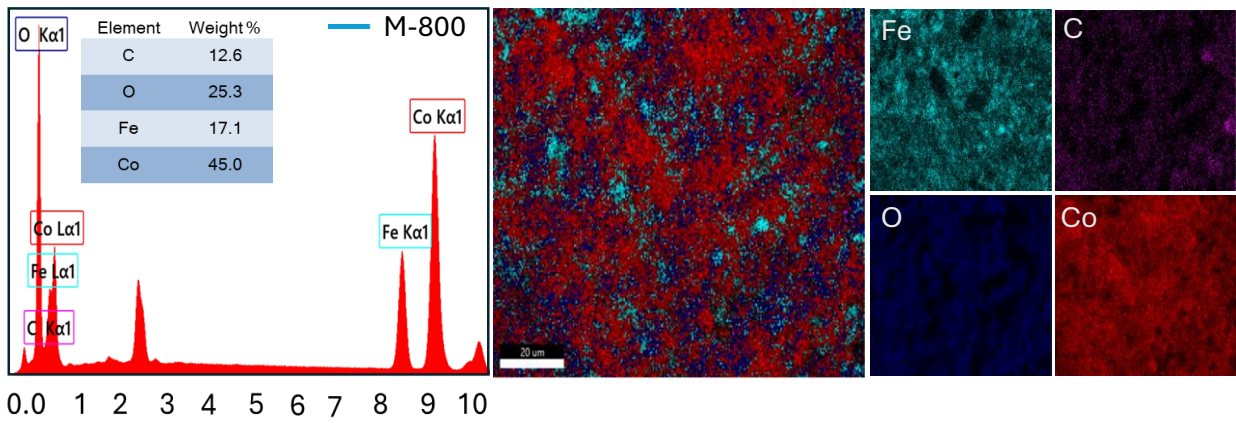


Figure 5.6.(d) EDX graphs of $\text{Co}_3\text{O}_4\text{:Fe-800}$.

5.7 TRANSMISSION ELECTRON MICROSCOPY (TEM)

Transmission electron microscopy (TEM) was employed to investigate the internal structural features of Co-MOF: Fe-derived Co_3O_4 : Fe-500 and the results are shown in Fig. 5.7(a). Co_3O_4 : Fe-500 showed chains of agglomerated spherical-shaped particles. The HR-TEM image of this sample is shown in Fig.5.7(b) disclosing the presence of crystallographic planes with interplanar spacing of 2.46 Å and 2.06 Å corresponding to (113) and (004) of Co_3O_4 , respectively. Furthermore, a plane with an interplanar spacing of 4.4 Å corresponds to a carbon peak. This is

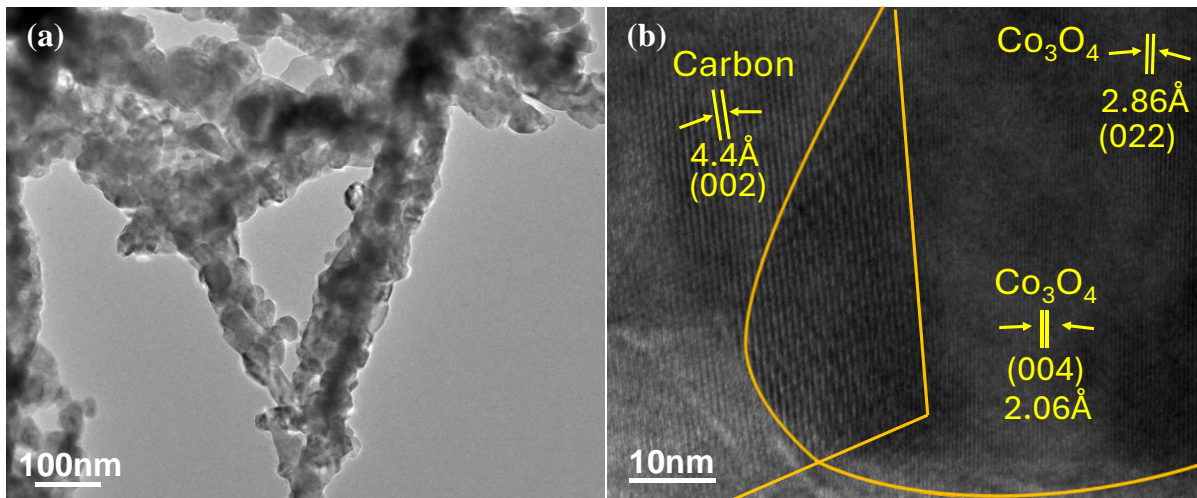


Figure 5.7. TEM and HR-TEM images of Co_3O_4 : Fe-500, confirming agglomerated spherical-shaped particles.

also supported by the EDX results as shown, supporting the XRD results.

5.8 BRUNAUER-EMMETT-TELLER (BET) RESULTS

The Brunauer-Emmett-Teller (BET) method was used to examine the surface area, pore size distribution, and pore volume of the synthesized Co-MOF: Fe, and MOF-derived Co_3O_4 : Fe-300, Co_3O_4 : Fe-500 and Co_3O_4 : Fe-800. The nitrogen adsorption/desorption isotherms and pore size plots of all the mentioned electrode materials are depicted in Fig. 5.8 (a-d). The isotherms of all the samples show a complete loop, indicating a conventional Type IV curve with an H3 hysteresis loop. Table (5.1) provides the surface area, pore size distribution, and pore volume of all four samples. BET surface area of Co-MOF: Fe, and derived Co_3O_4 : Fe at 300 °C, 500 °C, and 800 °C are as follows: 1.746 $\text{m}^2 \text{g}^{-1}$, 4.260 $\text{m}^2 \text{g}^{-1}$, 49.663 $\text{m}^2 \text{g}^{-1}$, and 13.575 $\text{m}^2 \text{g}^{-1}$ respectively. The result shows that the specific surface of MOF-derived Co_3O_4 : Fe increases with conversion temperature until 500 °C. A significant drop in BET surface area was observed as the temperature

was raised to 800 °C. The increase in the specific surface area with conversion temperature can be attributed to the need for a larger surface area to facilitate the decomposition of BDC present in the MOF during conversion. Conversely, the reduction of surface area while further increasing conversion temperature indicates the growth of already converted grains. The highest surface area of Co-MOF: Fe converted at 500 °C suggests the presence of more active sites. Additionally, the BJH pore diameter of these samples lies between 1.7000 nm and 300.0000 nm which further reveals their potential for catalytic applications. The high surface area and pore volume of the derived bimetallic doped oxide suggest that converting MOF into oxides increases the surface area, and pore volume while decreasing pore size.

Table 5.1. BET surface area, BJH pore size, pore volume, and BJH pore diameter of all synthesized materials.

Sample	BET Surface area (m²g⁻¹)	BJH Pore size (nm)	Pore volume (cm³g⁻¹)	BJH Pore diameter (nm)
Co-MOF:Fe	1.746	31.63014	10.053	5.68
Co ₃ O ₄ :Fe -300	4.260	18.746	20.008	2.89
Co ₃ O ₄ :Fe-500	49.663	7.514	230.184	1.78
Co ₃ O ₄ :Fe-800	13.575	16.038	30.058	2.59

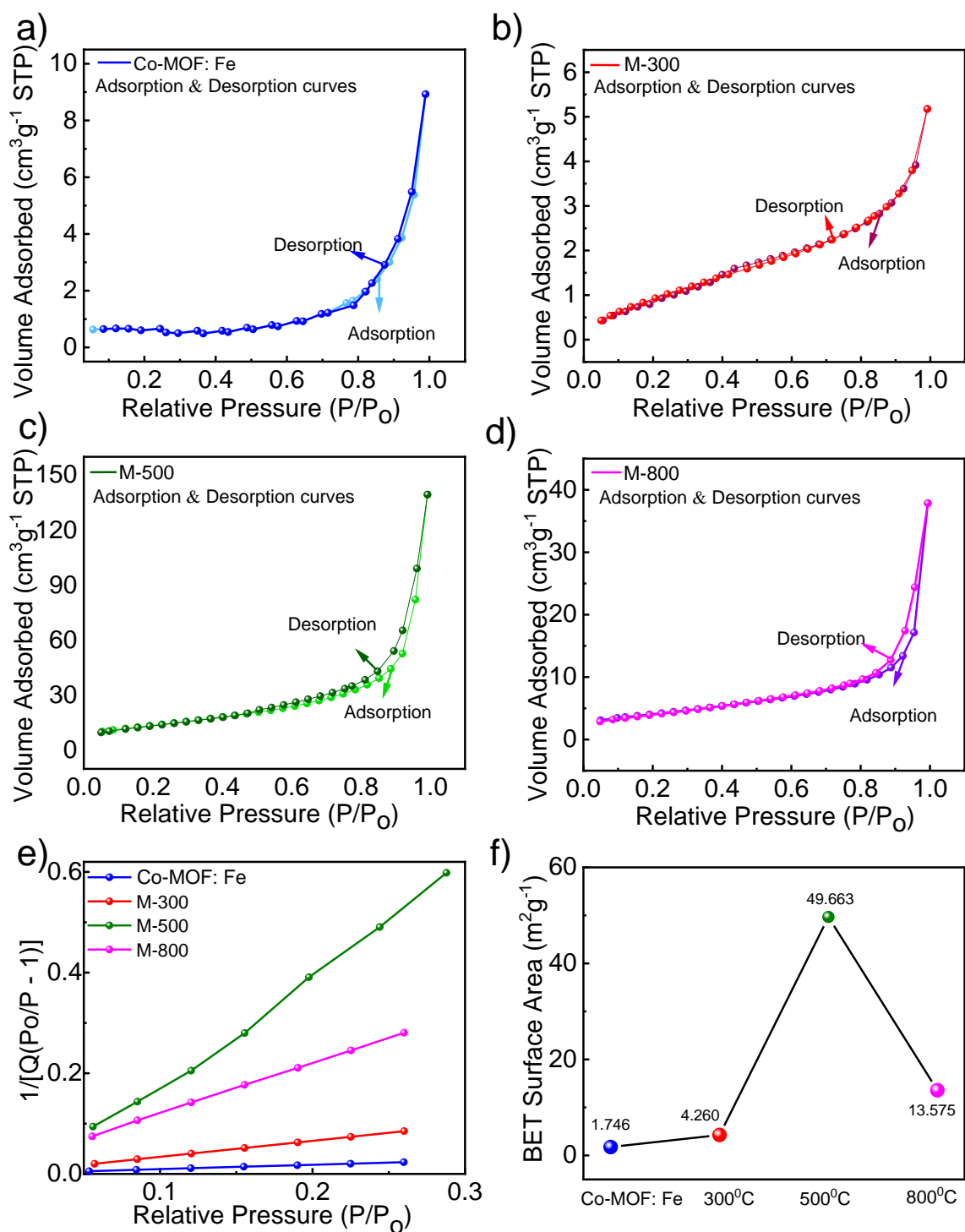


Figure 5.8.(a-e) Specific surface area and porosity of Co-MOF: Fe and derived Co_3O_4 : Fe at 300°C, 500°C, and 800°C were studied through BET analysis; (f) comparison plot of BET surface area of all the four mentioned electrodes.

5.9 GALVANOSTATIC CHARGE-DISCHARGE (GCD)

Galvanostatic charge-discharge (GCD) measurements were carried out to examine the charge-discharge properties of electrode materials for supercapacitors. GCD analysis was conducted at various current densities (1-5 mA) to measure the rate capability of the synthesized electrode materials while maintaining a specific potential limit; the obtained results are depicted in Fig. 5.9 (a-d). A comparison of these electrode materials is also provided in Fig. 5.9 (e) at a current density of 1 A g^{-1} . A non-linear behavior with prominent peaks in galvanic profiles demonstrates Faradaic reactions between the ions and the electrode. The corresponding behavior of the galvanostatic peaks shows the reversibility of redox reactions. The calculated Q_s values at a current density of 1 A/g for Co-MOF: Fe, derived Co_3O_4 : Fe at 300°C , 500°C , and 800°C were found to be 101.25 F g^{-1} , 270.22 F g^{-1} , 2135.08 F g^{-1} , and 936.25 F g^{-1} , respectively. Co_3O_4 : Fe-500 exhibited the best electrochemical performance, showing a longer discharge duration than the other electrodes i.e., pure Co-MOF: Fe and Co_3O_4 : Fe-300 and Co_3O_4 : Fe-800. The superior performance of Co_3O_4 : Fe-500 can be explained by its larger surface area, higher pore volume, and enhanced redox activity. These results suggest that the conversion of Co-MOF: Fe into derived Co_3O_4 : Fe oxide requires an optimized temperature for better energy storage capacity as supercapacitor electrode material.

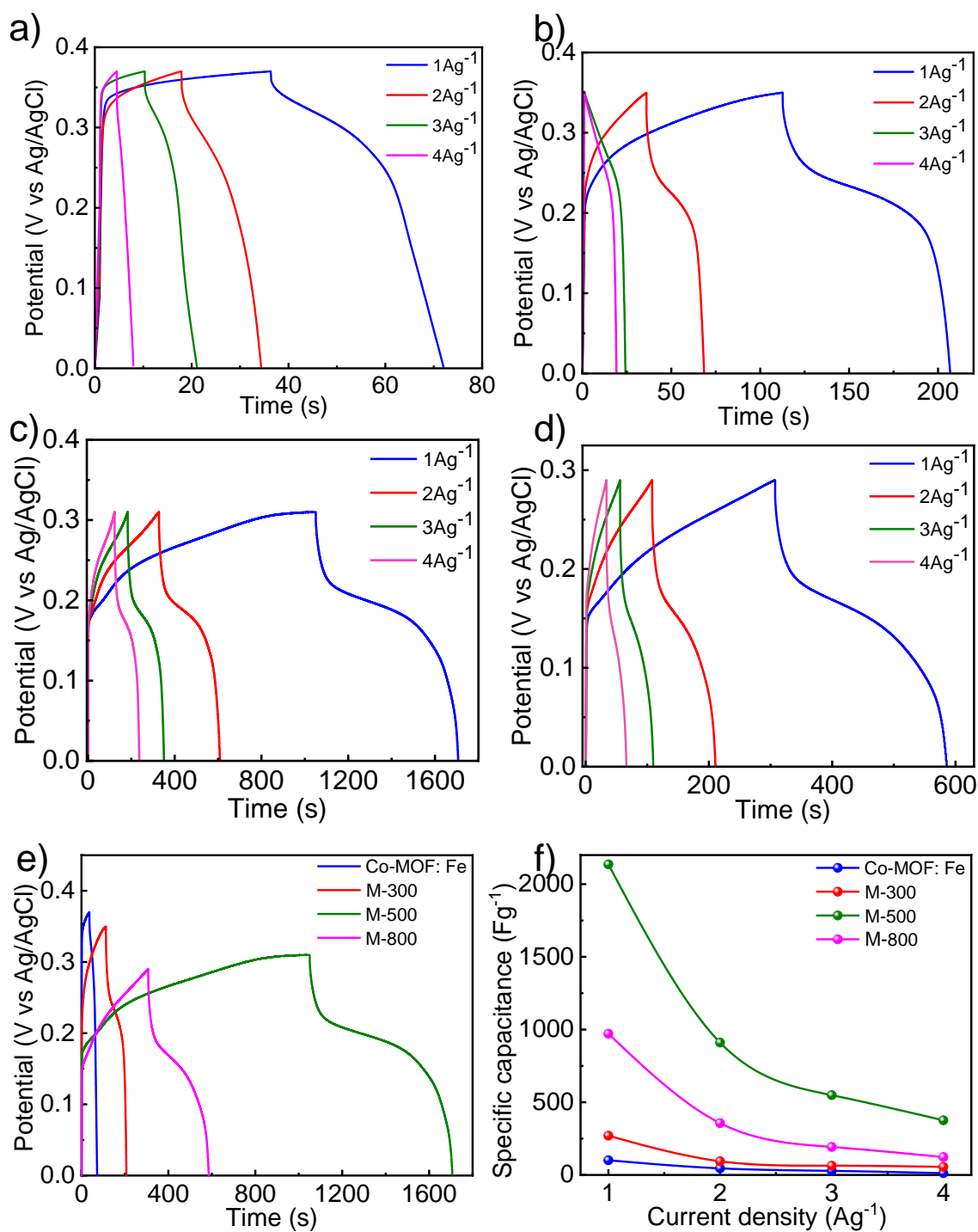


Figure 5.9. Electrochemical studies of the Co-MOF: Fe and derived Co₃O₄: Fe-300, Co₃O₄: Fe-500, and Co₃O₄: Fe-800 as supercapacitor electrode materials. (a-d) GCD profiles of the Co-MOF: Fe and derived Co₃O₄: Fe-300, Co₃O₄: Fe-500, and Co₃O₄: Fe-800 at specific current from 1 A g⁻¹ to 4 A g⁻¹; (e) comparison of GCD profile of all the mentioned electrode at specific current of 1 A g⁻¹. (f) Ragone plot displaying the current density vs specific capacitance of the mentioned supercapacitor electrodes.

5.10 CYCLIC VOLTAMMETRY (CV)

The electrochemical properties of the fabricated electrodes were studied using cyclic voltammetry (CV). The CV responses of the electrode materials were recorded at various scan rates ranging from 5 to 100 mV s^{-1} , as shown in Fig. 5.10(a-d). The potential range for CV was taken as their GCD potential window for understanding the charge storage mechanism. Co-MOF: Fe and derived Co_3O_4 : Fe at 300°C showed slight redox activity at low scan rates due to reduced metal ion accessibility in pure MOF, and incomplete phase change in derived oxide at 300°C. Furthermore, the redox activity diminishes as the sweep rate increases indicating the slow electron transfer kinetics and inhibition of the ion diffusion (Fig. 5.10 (a, b)). Fig. 5.10 (c, d), represents CV curves of MOF-derived oxides at 500°C and 800°C respectively, showing distinct redox peaks at various scan rates. The appearance of well-defined redox peaks indicates the better redox properties of oxides as compared to MOF. Fig. 5.10 (e) shows the CVs comparison of all the electrode materials at a scan rate of 10 mV/s . These results show that the area under the CV curves was found maximum for Co_3O_4 : Fe-500 followed by Co_3O_4 : Fe-800, Co_3O_4 : Fe-300, and Co-MOF: Fe, respectively. This can be explained by the greater redox activity of Co_3O_4 : Fe-500 due to its enhanced surface area than Co_3O_4 : Fe-800. The specific capacitance (Q_s) value of all the electrode materials was calculated from the cyclic voltammograms. The obtained Q_s value (@10 mV/s) of Co-MOF: Fe and derived Co_3O_4 : Fe at 300°C, 500°C, and 800 °C are 142.86, 277.77, 948.27, and 431.03 F/g, respectively. The results indicate the potential of derived Co_3O_4 : Fe at 500°C as an efficient electrode material due to high surface area, enhanced redox activity, and high Q_s value. The specific capacitance of all supercapacitor electrode material at scan rates of 5 mV/s , 10 mV/s , 20 mV/s , 40 mV/s , 60 mV/s , 80 mV/s , and 100 mV/s is depicted in Fig. 5.10 (f). These plots indicate that the Q_s value decreases with increasing sweep rate, suggesting the limiting interaction of ions and electrode materials with the rise in sweep rate.

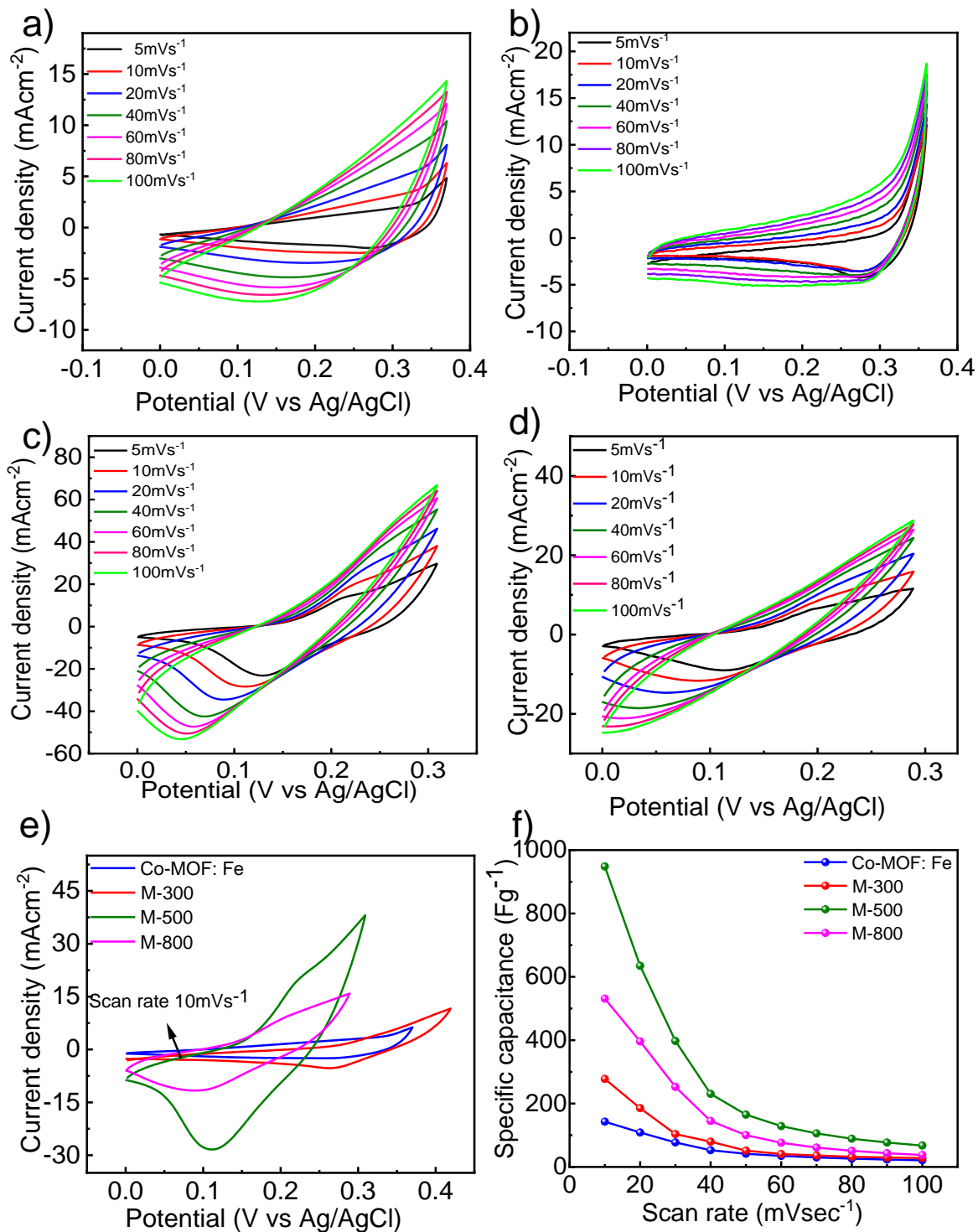


Figure 5.10.(a-d) CV curves of the Co-MOF: Fe and derived Co₃O₄: Fe-300, Co₃O₄: Fe-500, and Co₃O₄: Fe-800 as supercapacitor electrode materials at different scan rates from 5 to 100 mV s⁻¹; (e) comparison of CV curves of all the electrode material at a scan rate of 10 mV s⁻¹; (f) displaying specific capacitance vs scan rate plots of Co-MOF: Fe and derived Co₃O₄: Fe-300, Co₃O₄: Fe-500, and Co₃O₄: Fe-800.

5.11 ELECTROCHEMICAL IMPEDANCE SPECTROSCOPY (EIS)

Electrochemical impedance spectroscopy (EIS) analysis was carried out to understand the conductive behavior of the electrode materials in a frequency range of 0.1 to 100 kHz. The Nyquist plots along the fitted circuits for Co-MOF: Fe, Co₃O₄: Fe-300, Co₃O₄: Fe -500, and Co₃O₄: Fe e-800 are displayed in Fig. 5.11(a). All the electrode materials showed a single semicircle starting from the origin indicating negligible solution resistance. The diameter of these semicircles was used to calculate the charge transfer resistance (R_{ct}) which was found to be 1.779, 1.727, 0.507, and 0.943 ohms for Co-MOF: Fe, Co₃O₄: Fe-300, Co₃O₄: Fe-500, and Co₃O₄: Fe-800, respectively. The smallest charge transfer resistance of Co₃O₄: Fe-500 can be explained by the enhanced specific surface area and optimized porosity of this sample, which improve electrolyte accessibility to the nanostructured materials.

The key parameters that demonstrate the electrochemical performance of supercapacitor devices are cycle stability, Coulombic efficiency, energy (ED), and power density (PD). In this study, the cycle stability of all fabricated electrodes was analyzed up to 2000 cycles at a current density of 5A g⁻¹. The capacitance retention of the electrode materials was found in the following order: Co₃O₄: Fe -500 (96%) > Co₃O₄: Fe -800 (86%) > Co₃O₄: Fe -300 (85%) > Co-MOF: Fe -MOF (84%) (Fig. 5.10 (b)). The observed results directly correlate with the specific surface area and the charge transfer resistance values found for these electrodes. The enhanced surface area corresponds to increased active sites while low charge transfer resistance facilitates the process of energy storage and release. Therefore, the highest specific surface area and lowest charge transfer resistance of Co₃O₄: Fe -500 resulted in its superior capacitance retention. To further demonstrate the cyclic stability of Co₃O₄: Fe e-500, the capacitance retention was measured for 10,000 cycles. Notably, Co₃O₄: Fe -500 demonstrates remarkable stability with a capacitance retention of 87% after 10,000 cycles and a Coulombic efficiency of 99% (Fig. 5.11 (d)). The power density of the fabricated electrode materials was found to be 510.16 kW/kg, 502.77 kW/kg, 975.17 kW/kg, and 487.76 kW/kg for Co-MOF: Fe, Co₃O₄: Fe -300, Co₃O₄: Fe -500, and Co₃O₄: Fe -800, respectively

while possessing energy density of 5.06 Wh/kg, 13.13 Wh/kg, 103.788 Wh/kg and 37.71 Wh/kg respectively at current density of 1 A/g as shown in Fig. 5.11 (c).

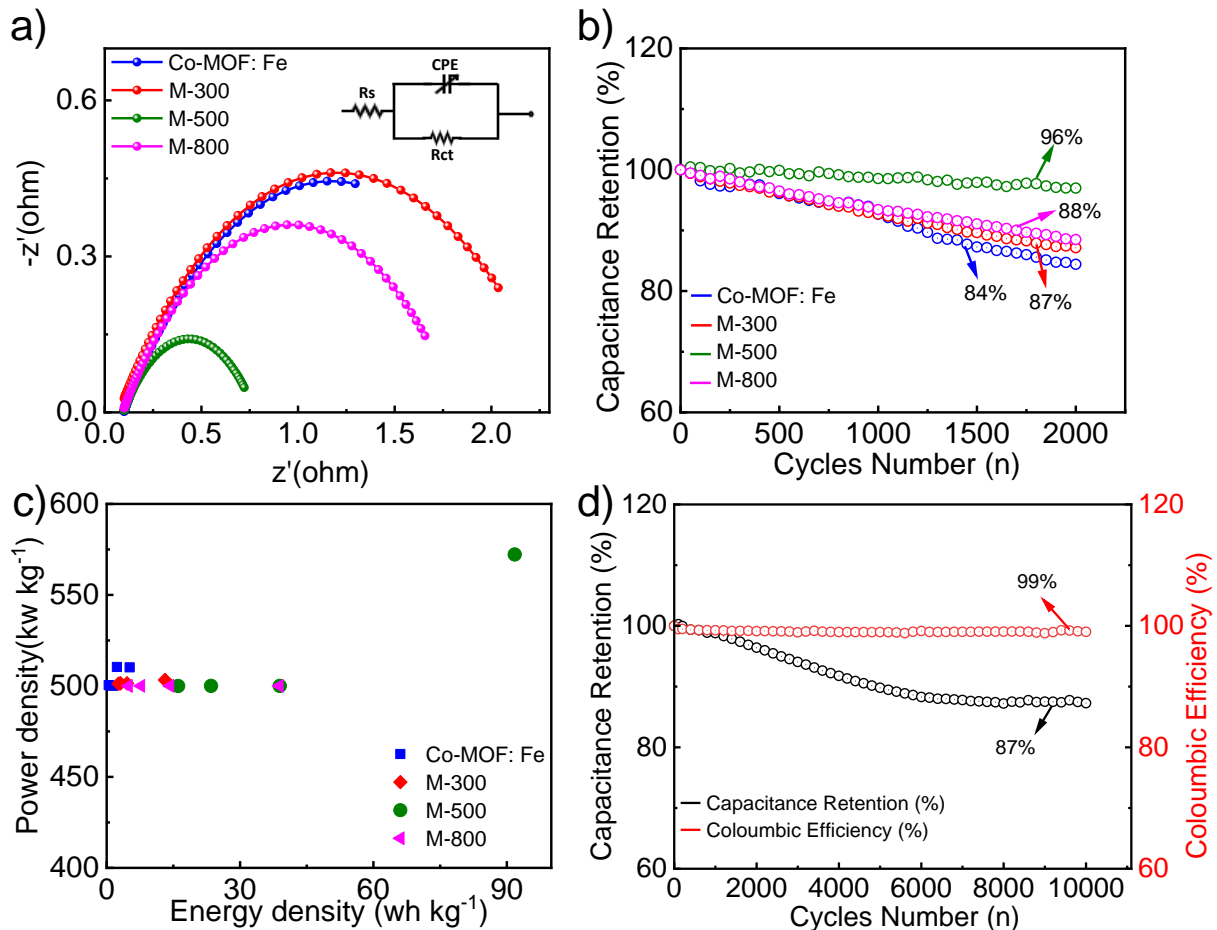


Figure 5.11.(a)Electrochemical impedance spectroscopy (EIS) of Co-MOF: Fe and its derivatives: Co_3O_4 : Fe-300, Co_3O_4 : Fe-500, and Co_3O_4 : Fe-800; (b) Cycling stability of these electrodes at 5 A g^{-1} for ~2000 cycles; (c) Ragone plot displaying the specific energy and power density of all the fabricated electrodes; (d) Cycling stability and Coloumbic efficiency of Co_3O_4 : Fe-500 for ~10000 cycles.

5.12 HYBRID DEVICE

We constructed a hybrid device (asymmetric device) using Co_3O_4 : Fe as anode and activated carbon as cathode to demonstrate the performance of the synthesized supercapacitor electrode material (Fig.5.12(a)). The Whatman paper was used as a separator to prevent short-circuiting by

physically separating the electrodes while allowing ion conduction through the electrolyte. The prepared electrodes were electrochemically activated at different potential windows: 0-0.6 V for $\text{Co}_3\text{O}_4\text{:Fe-500}$ and -1 to 0 V for activated carbon. The obtained cyclic profile of the device is presented in Fig. 5.12(b) at various scan rates ($10\text{--}100\text{ mVs}^{-1}$). The cyclic profile shows quasi-rectangular behavior elucidating the faradic nature of $\text{Co}_3\text{O}_4\text{:Fe-500}$ anode and non-Faradic-nature of activated carbon. The cyclic voltammograms maintained their shape even at the high scan rates indicating the remarkable rate capability of the hybrid device. The galvanostatic charge-discharge performance of the hybrid device was conducted at various current densities (1 to 4 A g^{-1}) as shown in Fig. 5.12 (c). The galvanostatic profile of the device also exhibited non-linear behavior, with a hump related to redox reactions and a triangular behavior demonstrating capacitive nature. These results indicate the presence of both reversible electric double-layer and pseudo-capacitor behavior. The device achieved Q_s of 233.98 F/g, 155.61 F/g, 101.89 F/g and 79.66 F/g at the corresponding current density of 1,2,3, and 4 A/g , respectively (Fig. 5.12 (d)).

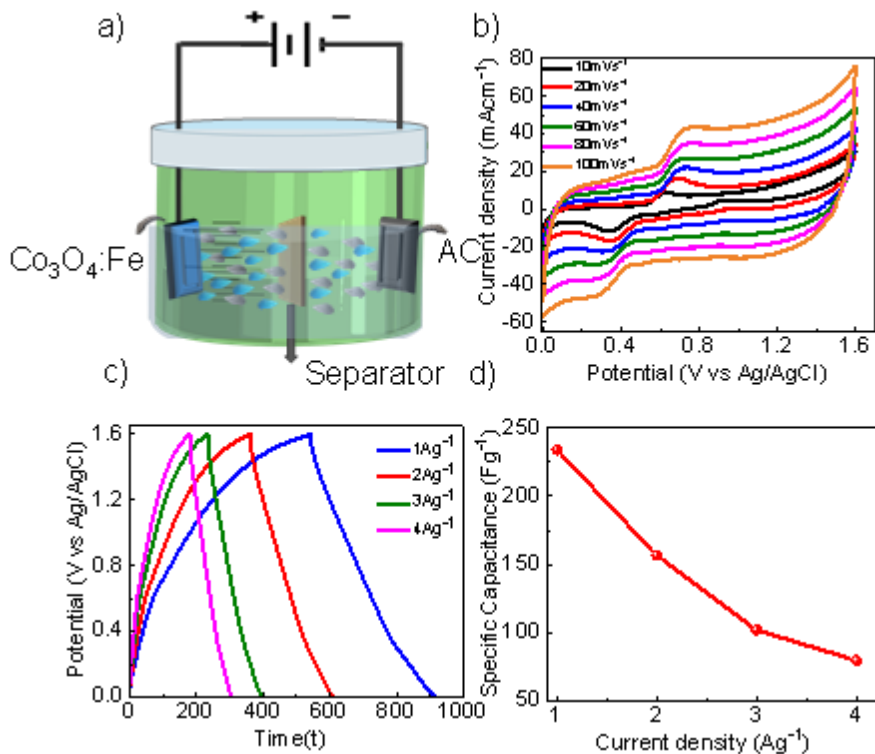


Figure 5.12.(a) Schematic illustration asymmetric device based on the activated carbon as cathode and the $\text{Co}_3\text{O}_4\text{:Fe}$ as anode; (b) CV-curves of derived $\text{Co}_3\text{O}_4\text{:Fe-500//AC}$ at different scan rate from 10 mV s^{-1} to 100 mV s^{-1} ; (c) GCD profiles of the $\text{Co}_3\text{O}_4\text{:Fe-500//AC}$ at different specific current from 1 to 4 A g^{-1} ; (d) specific capacitance vs current density plot of the asymmetric device.

The long-term cycling stability of a hybrid device is an essential parameter, therefore, capacitance retention of the device for 10,000 cycles. The device showed an excellent capacitance retention of 89% after 10,000 cycles at a current density of 5 A g⁻¹ while maintaining a very high Coulombic efficiency of 99%. Furthermore, Fig. 5.13(a) shows the Nyquist plot of a full-cell device between 10–100 kHz frequency range. The hybrid device showed a low Rct value of 0.25 Ω indicating its high conductivity. The energy and power densities of the Asymmetric SCs device were calculated from galvanostatic discharge curves and are plotted in Fig. 5.13 (b). The hybrid device displayed a maximum energy density of 51.99 Wh kg⁻¹ and a power density of 500.14 kW kg⁻¹ at the current density of 1 A g⁻¹. (Fig. 5.13 (c, d)).

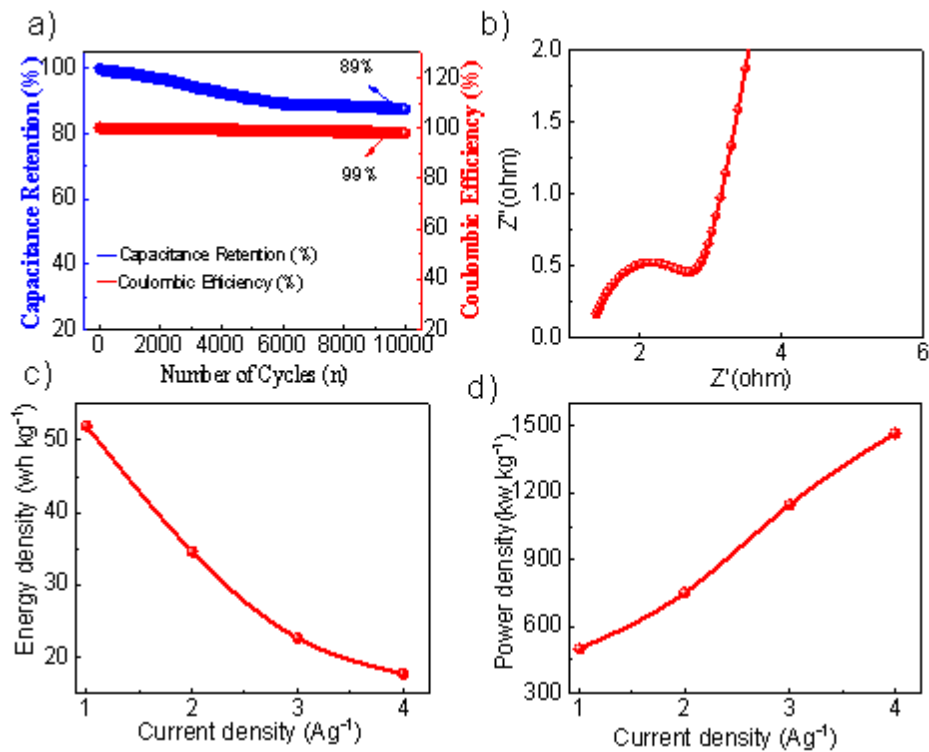


Figure 5.13.(a) Cycling test of Co₃O₄-500//AC device for 10000 cycles; (b) EIS of the Co₃O₄-500//AC device; (c) and (d) Ragone plot of Co₃O₄-500//AC asymmetric device.

CONCLUSION:

In this study, we successfully synthesized Co-MOF: Fe and derived Co₃O₄: Fe at 300°C, 500°C, and 800°C, and explored their potential as supercapacitor electrode materials. Our findings demonstrate that an optimized pyrolysis temperature is essential for better electrochemical properties of these materials. The derived Co₃O₄: Fe at 500 °C exhibited the highest specific capacity of 2135.08 F/g at 1 A/g and outstanding cycling stability of ~85% for 10000 cycles and ~ 99% Coulombic efficiency, making it a promising electrode material for high-performance supercapacitor application. The enhanced performance is attributed to the optimal thermal decomposition, high surface area, mesopores nature, and conductive network. To further access its practical applicability, a two-electrode asymmetric device was constructed using activated carbon, and the derived Co₃O₄:Fe at 500 °C as electrode materials. The hybrid device showed a specific capacitance of 233.98 F/g at 1 A/g, an energy density of ~51.99 Wh/kg, and a power density of 500.14 kW/kg. Furthermore, it maintained a remarkable capacitance retention of 89% for 10,000 cycles at a current density of 5 A./g which indicates the viability of the MOF-derived Co₃O₄:Fe for practical use in energy storage applications.

FUTURE RECOMMENDATION

- LSV (HER and OER) testing can be conducted to evaluate the water-splitting efficiency of the derived Co₃O₄:Fe electrocatalyst.
- Exploring other MOF-derived doped transition metal oxides can unveil novel opportunities for energy storage & water electrolyzers.

LIST OF PUBLICATION

“Tailoring the Electrochemical Performance of rods-like Co-MOF:Fe-Derived Co₃O₄:Fe Electrodes for Supercapacitor Applications,” (Journal of Fuel)

REFERENCES

- [1]J. Chen, P. Wang, L. Cui, S. Huang, M. Song, Decomposition and decoupling analysis of CO₂ emissions in OECD, *Applied Energy*. 231 (2018) 937–950.
- [2]K. Abbass, M.Z. Qasim, H. Song, M. Murshed, H. Mahmood, I. Younis, A review of the global climate change impacts, adaptation, and sustainable mitigation measures, *Environ Sci Pollut Res*. 29 (2022) 42539–42559.
- [3]R. Ali, I. Daut, S. Taib, A review on existing and future energy sources for electrical power generation in Malaysia, *Renewable and Sustainable Energy Reviews*. 16 (2012) 4047–4055.
- [4]G.W. Frey, D.M. Linke, Hydropower as a renewable and sustainable energy resource meeting global energy challenges in a reasonable way, *Energy Policy*. 30 (2002) 1261–1265.
- [5]I. Dincer, Renewable energy and sustainable development: a crucial review, *Renewable and Sustainable Energy Reviews*. 4 (2000) 157–175.
- [6]M. Yekini Suberu, M. Wazir Mustafa, N. Bashir, Energy storage systems for renewable energy power sector integration and mitigation of intermittency, *Renewable and Sustainable Energy Reviews*. 35 (2014) 499–514.
- [7]H. Ibrahim, A. Ilinca, J. Perron, Energy storage systems—Characteristics and comparisons, *Renewable and Sustainable Energy Reviews*. 12 (2008) 1221–1250.
- [8]A. Zahedi, Maximizing solar PV energy penetration using energy storage technology, *Renewable and Sustainable Energy Reviews*. 15 (2011) 866–870.
- [9]S. Rehman, L.M. Al-Hadhrami, Md.M. Alam, Pumped hydro energy storage system: A technological review, *Renewable and Sustainable Energy Reviews*. 44 (2015) 586–598.
- [10]M.Z. Iqbal, U. Aziz, Supercapattery: Merging of battery-supercapacitor electrodes for hybrid energy storage devices, *Journal of Energy Storage*. 46 (2022) 103823.
- [11]Q. Wang, S. Chen, D. Zhang, CNT yarn-based supercapacitors, in: *Carbon Nanotube Fibers and Yarns*, Elsevier, 2020: pp. 243–270.
- [12]J. Cherusseri, D. Pandey, J. Thomas, Symmetric, Asymmetric, and Battery-Type Supercapacitors Using Two-Dimensional Nanomaterials and Composites, *Batteries & Supercaps*. 3 (2020) 860–875.
- [13]S. S. Rangarajan, S.P. Sunddararaj, A. Sudhakar, C.K. Shiva, U. Subramaniam, E.R. Collins, T. Senjyu, Lithium-Ion Batteries—The Crux of Electric Vehicles with Opportunities and Challenges, *Clean Technol*. 4 (2022) 908–930.

- [14]Y. Han, Z. Lai, Z. Wang, M. Yu, Y. Tong, X. Lu, Designing Carbon Based Supercapacitors with High Energy Density: A Summary of Recent Progress, *Chem. Eur. J.* 24 (2018) 7312–7329.
- [15]P. Barrade, S. Delalay, A. Rufer, Direct Connection of Supercapacitors to Photovoltaic Panels With On–Off Maximum Power Point Tracking, *IEEE Trans. Sustain. Energy.* 3 (2012) 283–294.
- [16]F. Zhang, T. Zhang, X. Yang, L. Zhang, K. Leng, Y. Huang, Y. Chen, A high-performance supercapacitor-battery hybrid energy storage device based on graphene-enhanced electrode materials with ultrahigh energy density, *Energy Environ. Sci.* 6 (2013) 1623.
- [17]D.P. Chatterjee, A.K. Nandi, A review on the recent advances in hybrid supercapacitors, *J. Mater. Chem. A.* 9 (2021) 15880–15918.
- [18]P. Forouzandeh, V. Kumaravel, S.C. Pillai, Electrode Materials for Supercapacitors: A Review of Recent Advances, *Catalysts.* 10 (2020) 969.
- [19]Y. Ma, H. Chang, M. Zhang, Y. Chen, Graphene-Based Materials for Lithium-Ion Hybrid Supercapacitors, *Advanced Materials.* 27 (2015) 5296–5308.
- [20]C. An, Y. Zhang, H. Guo, Y. Wang, Metal oxide-based supercapacitors: progress and perspectives, *Nanoscale Adv.* 1 (2019) 4644–4658.
- [21]X. Li, A.M. Elshahawy, C. Guan, J. Wang, Metal Phosphides and Phosphates-based Electrodes for Electrochemical Supercapacitors, *Small.* 13 (2017) 1701530.
- [22]R. Barik, P.P. Ingole, Challenges and prospects of metal sulfide materials for supercapacitors, *Current Opinion in Electrochemistry.* 21 (2020) 327–334.
- [23]K.K. Gangu, S. Maddila, S.B. Mukkamala, S.B. Jonnalagadda, A review on contemporary Metal–Organic Framework materials, *Inorganic Chemical Acta.* 446 (2016) 61–74.
- [24]R. Grünker, V. Bon, P. Müller, U. Stoeck, S. Krause, U. Mueller, I. Senkovska, S. Kaskel, A new metal–organic framework with ultra-high surface area, *Chem. Commun.* 50 (2014) 3450.
- [25]H. Li, M. Eddaoudi, M. O’Keeffe, O.M. Yaghi, Design and synthesis of an exceptionally stable and highly porous metal-organic framework, *Nature.* 402 (1999) 276–279.
- [26]Z. Chen, K.O. Kirlikovali, P. Li, O.K. Farha, Reticular Chemistry for Highly Porous Metal–Organic Frameworks: The Chemistry and Applications, *Acc. Chem. Res.* 55 (2022) 579–591.
- [27]F. Béguin, E. Frackowiak, eds., *Supercapacitors: Materials, Systems, and Applications*, 1st ed., Wiley, 2013..
- [28]A. Muzaffar, M.B. Ahamed, K. Deshmukh, J. Thirumalai, A review on recent advances in hybrid supercapacitors: Design, fabrication and applications, *Renewable and Sustainable Energy Reviews.* 101 (2019) 123–145.
- [29]J. Tahalyani, M.J. Akhtar, J. Cherusseri, K.K. Kar, Characteristics of Capacitor: Fundamental Aspects, in: K.K. Kar (Ed.), *Handbook of Nanocomposite Supercapacitor Materials I*, Springer International Publishing, Cham, 2020: pp. 1–51.

- [30]M.E. Fouda, A. Allagui, A.S. Elwakil, S. Das, C. Psychalinos, A.G. Radwan, Nonlinear charge-voltage relationship in constant phase element, *AEU - International Journal of Electronics and Communications*. 117 (2020) 153104.
- [31]Q. Ke, J. Wang, Graphene-based materials for supercapacitor electrodes – A review, *Journal of Materiomics*. 2 (2016) 37–54.
- [32]Y. Rangom, X. (Shirley) Tang, L.F. Nazar, Carbon Nanotube-Based Supercapacitors with Excellent ac Line Filtering and Rate Capability *via* Improved Interfacial Impedance, *ACS Nano*. 9 (2015) 7248–7255.
- [33]B.K. Kim, S. Sy, A. Yu, J. Zhang, Electrochemical Supercapacitors for Energy Storage and Conversion, in: J. Yan (Ed.), *Handbook of Clean Energy Systems*, John Wiley & Sons, Ltd, Chichester, UK, 2015: pp. 1–25.
- [34]W. Raza, F. Ali, N. Raza, Y. Luo, K.-H. Kim, J. Yang, S. Kumar, A. Mehmood, E.E. Kwon, Recent advancements in supercapacitor technology, *Nano Energy*. 52 (2018) 441–473.
- [35]Huang, P.-L., et al., Ionic liquid electrolytes with various constituent ions for graphene-based supercapacitors. *Electrochimica Acta*, 2015. 161: p. 371-377.
- [36]Kumbhar, V., et al., Porous network of samarium sulfide thin films for supercapacitive application. *Materials Science in Semiconductor Processing*, 2015. 33: p. 136-139.
- [37]Wang, G., L. Zhang, and J. Zhang, A review of electrode materials for electrochemical supercapacitors. *Chemical Society Reviews*, 2012. 41(2): p. 797-828.
- [38]Iqbal, M.Z. and J.J.E.A. Khan, Optimization of cobalt-manganese binary sulfide for high performance supercapattery devices. 2021. 368: p. 137529.
- [39]Tan, Y., et al., Supercapacitor electrode of nano-Co₃O₄ decorated with gold nanoparticles via in-situ reduction method. *Journal of Power Sources*, 2017. 363: p. 1-8.
- [40]Zhi, M., et al., Nanostructured carbon–metal oxide composite electrodes for supercapacitors: a review. *Nanoscale*, 2013. 5(1): p. 72-88.
- [41]Sharma, K., A. Arora, and S.K. Tripathi, Review of supercapacitors: Materials and devices. *Journal of Energy Storage*, 2019. 21: p. 801-825.
- [42]Jänes, A., H. Kurig, and E. Lust, Characterisation of activated nanoporous carbon for supercapacitor electrode materials. *Carbon*, 2007. 45(6): p. 1226-1233.
- [43]Vangari, M., T. Pryor, and L. Jiang, Supercapacitors: review of materials and fabrication methods. *Journal of Energy Engineering*, 2013. 139(2): p. 72-79.
- [44]Chen, X., R. Paul, and L.J.N.S.R. Dai, Carbon-based supercapacitors for efficient energy storage. 2017. 4(3): p. 453-489.
- [45]Jayalakshmi, M. and K. Balasubramanian, Simple capacitors to supercapacitors-an overview. *Int. J. Electrochem. Sci*, 2008. 3(11): p. 1196-1217.

- [46]Lokhande, P.E., U.S. Chavan, and A. Pandey, Materials and fabrication methods for electrochemical supercapacitors: overview. *Electrochemical Energy Reviews*, 2020. 3(1): p. 155-186.
- [47]Spyker, R.L. and R.M. Nelms, Classical equivalent circuit parameters for a double-layer capacitor. *IEEE transactions on aerospace and electronic systems*, 2000. 36(3): p. 829-836.
- [48]Sharma, P. and T. Bhatti, A review on electrochemical double-layer capacitors. *Energy conversion and management*, 2010. 51(12): p. 2901-2912.
- [49]Vangari, M., T. Pryor, and L.J.J.o.E.E. Jiang, Supercapacitors: review of materials and fabrication methods. 2013. 139(2): p. 72-79.
- [50]Li, J., et al., Three-dimensional nitrogen and phosphorus co-doped carbon quantum dots/reduced graphene oxide composite aerogels with a hierarchical porous structure as superior electrode materials for supercapacitors. 2019. 7(46): p. 26311-26325.
- [51]Zhu, Y., et al., Graphitic carbon quantum dots modified nickel cobalt sulfide as cathode materials for alkaline aqueous batteries. 2020. 12(1): p. 1-18.
- [52]Gao, H., S. Xin, and J.B. Goodenough, The origin of superior performance of Co (OH) 2 in hybrid supercapacitors. *Chem*, 2017. 3(1): p. 26-28.
- [53]Conway, B.E., Transition from “supercapacitor” to “battery” behavior in electrochemical energy storage. *Journal of the Electrochemical Society*, 1991. 138(6): p. 1539.
- [54]González, A., et al., Review on supercapacitors: Technologies and materials. *Renewable and Sustainable Energy Reviews*, 2016. 58: p. 1189-1206.
- [55]Kate, R.S., S.A. Khalate, and R.J. Deokate, Overview of nanostructured metal oxides and pure nickel oxide (NiO) electrodes for supercapacitors: A review. *Journal of Alloys and Compounds*, 2018. 734: p. 89-111.
- [56]Zhang, Y., et al., Progress of electrochemical capacitor electrode materials: A review. *International journal of hydrogen energy*, 2009. 34(11): p. 4889-4899.
- [57]Iqbal, M.Z., M.M. Faisal, and S.R.A.M.J.S.S.I. Alzaid, A facile approach to investigate the charge storage mechanism of MOF/PANI based supercapattery devices. 2020. 354: p. 115411.
- [58]Stoller, M.D., et al., Graphene-based ultracapacitors. *Nano letters*, 2008. 8(10): p. 3498-3502.
- [59]Y. Wang, L. Yu, Y. Xia, Electrochemical Capacitance Performance of Hybrid Supercapacitors Based on Ni(OH)₂/Carbon Nanotube Composites and Activated Carbon, *J. Electrochem. Soc.* 153 (2006) A743.
- [60]M. Lätt, M. Käärik, L. Permann, H. Kuura, M. Arulepp, J. Leis, A structural influence on the electrical double-layer characteristics of Al₄C₃-derived carbon, *J Solid State Electrochem.* 14 (2010) 543–548.

- [61]M.Z. Ullah Shah, M.S. Javed, M. Sajjad, A. Shah, M.S. Shah, S. ur Rahman, A. Mahmood, M.A. Ahmad, M.A. Assiri, H. Hou, A novel TiO₂/CuSe based nanocomposite for high-voltage asymmetric supercapacitors, *Journal of Science: Advanced Materials and Devices*. 7 (2022) 100418.
- [62]M.Z. Iqbal, U. Aziz, M.W. Khan, S. Siddique, M. Alzaid, S. Aftab, Strategies to enhance the electrochemical performance of strontium-based electrode materials for battery-supercapacitor applications, *Journal of Electroanalytical Chemistry*. 924 (2022) 116868.
- [63]N. Elgrishi, K.J. Rountree, B.D. McCarthy, E.S. Rountree, T.T. Eisenhart, J.L. Dempsey, A Practical Beginner's Guide to Cyclic Voltammetry, *J. Chem. Educ.* 95 (2018) 197–206.
- [64]P.T. Kissinger, W.R. Heineman, Cyclic voltammetry, *J. Chem. Educ.* 60 (1983) 702.
- [65]V.D. Parker, Chapter 3 Linear Sweep and Cyclic Voltammetry, in: *Comprehensive Chemical Kinetics*, Elsevier, 1986: pp. 145–202.
- [66]M.S. Javed, S. Dai, M. Wang, Y. Xi, Q. Lang, D. Guo, C. Hu, Faradic redox active material of Cu₇S₄ nanowires with a high conductance for flexible solid state supercapacitors, *Nanoscale*. 7 (2015) 13610–13618.
- [67]L. Jiang, J. Yan, L. Hao, R. Xue, G. Sun, B. Yi, High rate performance activated carbons prepared from ginkgo shells for electrochemical supercapacitors, *Carbon*. 56 (2013) 146–154.
- [68]A.F. Pérez-Torres, M. González-Hernández, P. Ortiz, M.T. Cortés, Statistical Study of the Influence of Electrosynthesis Conditions on the Capacitance of Polypyrrole, *ACS Omega*. 7 (2022) 15580–15595.
- [69]K.H. Oh, G.S. Gund, H.S. Park, Stabilizing NiCo₂O₄ hybrid architectures by reduced graphene oxide interlayers for improved cycling stability of hybrid supercapacitors, *J. Mater. Chem. A*. 6 (2018) 22106–22114.
- [70]X. Yang, A.L. Rogach, *Electrochemical Techniques in Battery Research: A Tutorial for Nonelectrochemists*, *Adv. Energy Mater.* 9 (2019) 1900747.
- [71]W.H. Low, S.S. Lim, C.W. Siong, C.H. Chia, P.S. Khiew, One dimensional MnV₂O₆ nanobelts on graphene as outstanding electrode material for high energy density symmetric supercapacitor, *Ceramics International*. 47 (2021) 9560–9568.
- [72]S. Grassini, S. Corbellini, M. Parvis, E. Angelini, F. Zucchi, A simple Arduino-based EIS system for in situ corrosion monitoring of metallic works of art, *Measurement*. 114 (2018) 508–514.
- [73]B.-A. Mei, O. Munteshari, J. Lau, B. Dunn, L. Pilon, Physical Interpretations of Nyquist Plots for EDLC Electrodes and Devices, *J. Phys. Chem. C*. 122 (2018) 194–206.
- [74]P.G. Bruce, S.A. Freunberger, L.J. Hardwick, J.-M. Tarascon, Li–O₂ and Li–S batteries with high energy storage, *Nature Mater.* 11 (2012) 19–29.

- [75]H. Zhang, Y. Zhou, Y. Ma, J. Yao, X. Li, Y. Sun, Z. Xiong, D. Li, RF magnetron sputtering synthesis of three-dimensional graphene@Co₃O₄ nanowire array grown on Ni foam for application in supercapacitors, *Journal of Alloys and Compounds*. 740 (2018) 174–179.
- [76]Mei, J., et al., Cobalt oxide-based nanoarchitectures for electrochemical energy applications. *Progress in Materials Science*, (2019). 103: p. 596-677.
- [77]Hua, Y., et al., Cobalt based metal-organic frameworks and their derivatives for electrochemical energy conversion and storage. *Chemical Engineering Journal*, (2019). 370: p. 37-59.
- [78]Qi, S., et al., Cobalt-based electrode materials for sodium-ion batteries. *Chemical Engineering Journal*, (2019). 370: p. 185-207.
- [79] Xu, J., et al., Preparation and electrochemical capacitance of cobalt oxide (Co₃O₄) nanotubes as supercapacitor material. *Electrochimica Acta - ELECTROCHIM ACTA*, (2010) 56: p. 732-736.
- [80]Chen, M., et al., Cobalt oxides nanorods arrays as advanced electrode for high performance supercapacitor. *Surface and Coatings Technology*, (2019). 360: p. 73-77.
- [81]Chen, T.-Y. and L.-Y. Lin, Morphology variation for the nickel cobalt molybdenum copper oxide with different metal ratios and their application on energy storage. *Electrochimica Acta*, (2019). 298: p. 745-755.
- [82]Poizot, P., et al., Nano-sized transition-metal oxides as negative-electrode materials for lithium-ion batteries. *Nature*, (2000). 407(6803): p. 496-499
- [83]Alcántara, R., et al., NiCo₂O₄ Spinel: First Report on a Transition Metal Oxide for the Negative Electrode of Sodium-Ion Batteries. *Chemistry of Materials*, (2002). 14(7): p. 2847-2848.
- [84]Yuan, Y.F., et al., Hierarchically porous Co₃O₄ film with mesoporous walls prepared via liquid crystalline template for supercapacitor application. *Electrochemistry Communications - ELECTROCHEM COMMUN*, (2011). 13: p. 1123-1126.
- [85]Kung, C.-W., et al., Synthesis of Co₃O₄ nanosheets via electrodeposition followed by ozone treatment and their application to high-performance supercapacitors. *Journal of Power Sources*, (2012). 214: p. 91-99.
- [86]Fan, Y., et al., Ultrathin Nanoflakes Assembled 3D Hierarchical Mesoporous Co₃O₄ Nanoparticles for High-Rate Pseudocapacitors. *Particle & Particle Systems Characterization*, (2014). 31(10): p. 1079-1083.
- [87]Zhang, G., et al., Nanoforest of hierarchical Co₃O₄@NiCo₂O₄ nanowire arrays for high-performance supercapacitors. *Nano Energy*, (2013). 2(5): p. 586-594.
- [88]Huang, M., et al., Facile synthesis of hierarchical Co₃O₄@MnO₂ core-shell arrays on Ni foam for asymmetric supercapacitors. *Journal of Power Sources*, (2014). 252: p. 98-106.

- [89]Huang, T., et al., Facilely synthesized porous ZnCo₂O₄ rodlike nanostructure for high-rate supercapacitors. *Ionics*, (2015). 21: p. 3109-3115.
- [90]Zhang, C., et al., Facile preparation of flower-like NiCo₂O₄/three dimensional graphene foam hybrid for high performance supercapacitor electrodes. *Carbon*, (2015). 89: p. 328-339.
- [91]Chen, H., et al., 3D hierarchically porous zinc–nickel–cobalt oxide nanosheets grown on Ni foam as binder-free electrodes for electrochemical energy storage. *Journal of Materials Chemistry A*, (2015). 3(47): p. 24022-24032.
- [92]Ma, W., et al., Superior performance asymmetric supercapacitors based on ZnCo₂O₄@MnO₂ core–shell electrode. *Journal of Materials Chemistry A*, (2015). 3(10): p. 5442-5448.
- [93]Xu, K., et al., Hierarchical mesoporous NiCo₂O₄@MnO₂ core–shell nanowire arrays on nickel foam for aqueous asymmetric supercapacitors. *Journal of Materials Chemistry A*, (2014). 2(13): p. 4795-4802.
- [94]Liu, X., J. Liu, and X. Sun, NiCo₂O₄@NiO hybrid arrays with improved electrochemical performance for pseudocapacitors. *Journal of Materials Chemistry A*, (2015). 3(26): p. 13900-13905.
- [95]Xu, Y., et al., Facile synthesis route of porous MnCo₂O₄ and CoMn₂O₄ nanowires and their excellent electrochemical properties in supercapacitors. *Journal of Materials Chemistry A*, (2014). 2(39): p. 16480-16488.
- [96]Xu, Y., et al., Mesoporous composite nickel cobalt oxide/graphene oxide synthesized via a template-assistant co-precipitation route as electrode material for supercapacitors. *Journal of Power Sources*, (2016). 306: p. 742-752.
- [97]Sahoo, S. and J.-J. Shim, Facile Synthesis of Three-Dimensional Ternary ZnCo₂O₄/Reduced Graphene Oxide/NiO Composite Film on Nickel Foam for Next Generation Supercapacitor Electrodes. *ACS Sustainable Chemistry & Engineering*, (2017). 5(1): p. 241-251.
- [98]Fang, L., et al., Hierarchical CoMoO₄ nanoneedle electrodes for advanced supercapacitors and electrocatalytic oxygen evolution. *Electrochimica Acta*, (2018). 259: p. 552-558.
- [99]Hu, W., et al., Flower-like nickel-zinc-cobalt mixed metal oxide nanowire arrays for electrochemical capacitor applications. *Journal of Alloys and Compounds*, (2017) 708: p. 146-153.
- [100]Wu, C., et al., Hybrid Reduced Graphene Oxide Nanosheet Supported Mn-Ni-Co Ternary Oxides for Aqueous Asymmetric Supercapacitors. *ACS applied materials & interfaces*, (2017). 9.
- [101]Zhao, J., et al., Hierarchical ferric-cobalt-nickel ternary oxide nanowire arrays supported on graphene fibers as high-performance electrodes for flexible asymmetric supercapacitors. *Nano Research*, (2018). 11(4): p. 1775-1786.
- [102]He, X., et al., Hierarchical FeCo₂O₄@NiCo layered double hydroxide core/shell nanowires for high performance flexible all-solid-state asymmetric supercapacitors. *Chemical Engineering Journal*, (2018). 334: p. 1573-1583.

- [103]Feng, H., et al., Construction of 3D hierarchical porous NiCo₂O₄/graphene hydrogel/Ni foam electrode for high-performance supercapacitor. *Electrochimica Acta*, (2019). 299: p. 116-124.
- [104]Iqbal, J., et al., Density functional theory simulation of cobalt oxide aggregation and facile synthesis of a cobalt oxide, gold and multiwalled carbon nanotube based ternary composite for a high performance supercapattery. 2019. 43(33): p. 13183-13195.
- [105]BoopathiRaja, R., M. Parthibavarman, and A.N.J.V. Begum, Hydrothermal induced novel CuCo₂O₄ electrode for high performance supercapacitor applications. 2019. 165: p. 96-104.
- [106]Li, G., et al., Self-templated formation of CuCo₂O₄ triple-shelled hollow microspheres for all-solid-state asymmetric supercapacitors. 2019. 787: p. 694-699.
- [107]Xiang, F., et al., An oxygen-deficient cobalt-manganese oxide nanowire doped with P designed for high performance asymmetric supercapacitor. *Electrochimica Acta*, 2021. 379: p. 138178.
- [108]Zhang, H., et al., Wire spherical-shaped Co-MOF electrode materials for high-performance all-solid-state flexible asymmetric supercapacitor device. *Journal of Alloys and Compounds*, 2021. 879: p. 160423.
- [109]Ma, Z., et al., Carbon nanotubes interpenetrating MOFs-derived Co-Ni-S composite spheres with interconnected architecture for high performance hybrid supercapacitor. 2021. 602: p. 627-635.
- [110]Bi, Q., et al., Hierarchical core-shell 2D MOF nanosheet hybrid arrays for high performance hybrid supercapacitors. *Dalton Transactions*, 2021. 50(23): p. 8179-8188.
- [111]Nagaraju, G., et al., High-performance hybrid supercapacitors based on MOF-derived hollow ternary chalcogenides. *Energy Storage Materials*, 2021. 35: p. 750-760.
- [112]Zhang, H., et al., Wire spherical-shaped Co-MOF electrode materials for high performance all-solid-state flexible asymmetric supercapacitor device. 2021. 879: p. 160423.
- [113]Javed, M.S., et al., An ultra-high energy density flexible asymmetric supercapacitor based on hierarchical fabric decorated with 2D bimetallic oxide nanosheets and MOF-derived porous carbon polyhedra. *Journal of Materials Chemistry A*, 2019. 7(3): p. 946-957.

- [114] Iqbal, M.Z., et al., Cobalt-oxide/carbon composites for asymmetric solid-state supercapacitors. 2020. 131: p. 110974.
- [115] S. Gao, Y. Sui, F. Wei, J. Qi, Q. Meng, Y. Ren, Y. He, Dandelion-like nickel/cobalt N metal-organic framework based electrode materials for high performance supercapacitors, *Journal of Colloid and Interface Science*. 531 (2018) 83–90. <https://doi.org/10.1016/j.jcis.2018.07.044>.
- [116] G. Zhu, H. Wen, M. Ma, W. Wang, L. Yang, L. Wang, X. Shi, X. Cheng, X. Sun, Y. Yao, A self-supported hierarchical Co-MOF as a supercapacitor electrode with ultrahigh areal capacitance and excellent rate performance, *Chem. Commun.* 54 (2018) 10499–10502. <https://doi.org/10.1039/C8CC03669A>.
- [117] S. Xu, R. Liu, X. Shi, Y. Ma, M. Hong, X. Chen, T. Wang, F. Li, N. Hu, Z. Yang, A dual CoNi MOF nanosheet/nanotube assembled on carbon cloth for high performance hybrid supercapacitors, *Electrochimica Acta*. 342 (2020) 136124.
- [118] “China Teflon Lined Hydrothermal Synthesis Autoclave Acid Digestion Reactor Manufacturers, Suppliers and Factory - Toption Instrument Co.,Ltd.” Accessed: Oct. 17, 2023.
- [119] “Supply BIOBASE Electric Forced Air Drying Oven Laboratory Wholesale Factory - BIOBASE GROUP.” Accessed: Oct. 17, 2023.
- [120] “[Benchmark Scientific] LC-8 Series Laboratory Centrifuges - General Purpose Centrifuges - CENTRIFUGES.” Accessed: Oct. 17, 2023. LaboratoryCentrifuges/1741 [69] “Powder X-ray Diffractometer (XRD) – CMS – Center Material Science Equipment.” Accessed: Oct. 17, 2023.
- [121] “FTIR : Principle, Instrumentation, Applications, Advantages,.” Accessed: Oct. 17, 2023.
- [122] Downes, A. & Elfick, A. Raman spectroscopy and related techniques in biomedicine. *Sensors* 10, 1871–1889 (2010).
- [123] N. Baig, I. Kammakakam, W. Falath, and I. Kammakakam, “Nanomaterials: A review of synthesis methods, properties, recent progress, and challenges,” *Materials Advances*, vol. 2, no. 6. Royal Society of Chemistry, pp. 1821–1871, Mar. 21, 2021.
- [124] “Evaluation of materials using scanning electron microscope (SEM) | The global standard for mixing, defoaming, dispersing, and pulverizing THINKY CORPORATION.” Accessed: Oct. 17, 2023.
- [125] “EDX | Energy Dispersive x-ray-elemental analysis | Mason Technology.” Accessed: Oct. 17, 2023.
- [126] Abdel Maged, F., Shawkey, H. A., Rayan, D. A. & Turky, G. M. Comparative study of CdS&TiO₂ based polyaniline/polyvinyl alcohol nanocomposites as electrode for supercapacitors. *Phys Scr* 97, (2022)